9-10-2009

Dissecting Galaxy Formation. I. Comparison Between Pure Dark Matter and Baryonic Models

Emilio Romano-Diaz
Argelander Institute for Astronomy, emiliord@astro.uni-bonn.de

Isaac Shlosman
University of Kentucky, isaac.shlosman@uky.edu

Clayton Heller
Georgia Southern University, cheller@georgiasouthern.edu

Yehuda Hoffman
Hebrew University of Jerusalem, hoffman@huji.ac.il

TO BE PUBLISHED BY THE ASTROPHYSICAL JOURNAL
Preprint typeset using LaTeX style emulateapj v. 6/22/04

DISSECTING GALAXY FORMATION: I. COMPARISON BETWEEN PURE DARK MATTER AND BARYONIC MODELS

EMILIO ROMANO-DÍAZ[1], ISAAC SHLOSMAN[2,3], CLAYTON HELLER[4], YEHUDA HOFFMAN[5]

to be published by the Astrophysical Journal

ABSTRACT

We compare assembly of dark matter (DM) halos with and without baryons from identical initial conditions, within the context of cosmological evolution in the ΛCDM WMAP3 Universe (baryons+DM, hereafter BDM model, and pure DM, PDM model). In representative PDM and BDM models we find that baryons contribute decisively to the evolution of the central region, leading to an isothermal DM cusp, and thereafter to a flat DM density core — the result of heating by dynamical friction of the DM+baryon substructure during a quiescent evolution epoch. This process ablates the cold gas from an embedded disk, cutting the star formation rate by a factor of 10, and heats up the spheroidal gas and stellar components, triggering their expansion. The substructure is more resilient to the tidal disruption in the presence of baryons. The disk which formed from inside-out as gas-dominated, is transformed into an intermediate Hubble type by $z \sim 2$ and to an early type by $z \sim 0.5$, based on its gas contents and spheroidal-to-disk stellar mass ratio. We find that only a relatively small $\sim 20\%$ fraction of DM particles in PDM and BDM models are bound within the radius of maximal circular velocity in the halo, slightly less so within halo characteristic radii — most of the DM particles perform larger radial excursions. The DM particles are unbound to the cusp region. We also find that the fraction of baryons within the halo virial radius somewhat increases during the major mergers and decreases during the minor mergers. The net effect appears to be negligible — an apparent result of our choice of feedback from stellar evolution. Furthermore, we find that the DM halos are only partially relaxed beyond their virialization. While the substructure is being tidally-disrupted, mixing of its debris in the halo is not efficient and becomes even less so with z. The phase-space correlations (streamers) formed after $z \sim 1$ will survive largely to the present time — an important implication for embedded disk evolution.

Subject headings: cosmology: dark matter — galaxies: evolution — galaxies: formation — galaxies: halos — galaxies: interactions — galaxies: kinematics and dynamics

1. INTRODUCTION

Luminous parts of galaxies are known to form inside dark matter (DM) halos (e.g., White & Rees 1978). Within the CDM paradigm, baryons are well mixed with DM initially. The collapse and virialization of DM is accompanied by infall of the baryonic matter. Dissipation results in the partial separation between these components — a process which can be slowed down by gas-to-stars conversion in ellipticals and by the angular momentum barrier in disk galaxies. This separation can lead to a number of processes which amplify the angular momentum and energy transfer between DM and baryons when the latter accumulate in the central region of the potential well. Understanding these processes is of prime importance because galaxy evolution is largely driven by mass, energy and angular momentum flows.

Within the framework of the CDM WMAP3 cosmology (Spergel et al. 2003, 2007), the baryons account for non-negligible, $\sim 17\%$, mass fraction. It is important to ask, therefore, what effect the baryons have on the DM halo evolution and vice versa. The main issue which we attempt to address here and in the companion paper (Romano-Diaz et al., in preparation, Paper II) is to what degree the DM halo, its buildup and relaxation, as well as properties and evolution of the surrounding substructure are affected by the baryons. Consequently, we explore in depth the baryon aspects of DM dynamics in the halo. We follow the baryon evolution as gas and stars which subject the system to energy and momentum feedbacks. Contrary to the statistical approach prevailing in the field, which aims at typical properties of growing halos, we focus on a small number of models which start from identical initial conditions. The models differ only by the presence or absence of baryons, hereafter baryons+DM (BDM model) and pure DM (PDM). As a prototype, we choose a massive Milky Way-type halos which have experienced an early epoch of major mergers, but remained isolated since $z \sim 1.5$.

The scope of baryon–DM interactions in context of galaxy evolution has been explored directly and indirectly over some time (e.g., Shlosman 2007 and refs. therein). For example, the halos appear to have small angular momentum compared to baryons in disks. As a result, the angular momentum can naturally flow from the disk to the surrounding halo, especially if triggered by lack of axial symmetry (e.g., Lynden-Bell & Kalnajs 1972; Tremaine & Weinberg 1984; Debattista & Sellwood 1998; Athanassoula & Misiriotis 2002; Athanassoula 2002; Martinez-Valpuesta, Shlosman & Heller 2006).

[1] Department of Physics and Astronomy, University of Kentucky, Lexington, KY 40506-0055, USA
[2] JILA, University of Colorado, Boulder, CO 80309-0440, USA
[3] National Institute of Standards and Technology, Boulder, CO 80305-3328, USA
[4] Department of Physics, Georgia Southern University, Statesboro, GA 30460, USA
[5] Racah Institute of Physics, Hebrew University; Jerusalem 91904, Israel

Hence, triaxial shapes of DM halos consistently obtained in pure DM cosmological simulations (e.g., Allgood et al. 2006) are expected to facilitate such an angular momentum transfer from baryons, despite the latter ability to lower this triaxiality (Kazantzidis et al. 2004; Berentzen & Shlosman 2006).

One cannot understand the full extent of baryon-DM interactions without in-depth analysis of the dynamical state of DM in a pure DM halo. This, however, has encountered a number of difficulties. We do not understand the origin of some of the seemingly most robust parameters defining the halo properties, such as the density profiles (e.g., Navarro, Frenk & White 1997, hereafter NFW; El-Zant 2008), the phase-space density profiles (e.g., Taylor & Navarro 2001; Hoffman et al. 2007), and the density slope – velocity anisotropy relation (e.g., Hansen & Moore 2006; Barnes et al. 2007; Zait, Hoffman & Shlosman 2008), and others. Which parameters are the most important ones in characterizing the growing halo is currently debatable. What is the relevance of the characteristic (NFW) radius $R_{\rm s}$? As this parameter is obtained by spherically-symmetrizing the halos, what significance it has for arbitrary-shaped halos is not clear.

Furthermore, while an assembling halo goes through the virialization process, its relaxation both in the configuration and velocity spaces is not well understood. The existence of substructure (e.g., subhalos) within the context of the hierarchical clustering is inherent and subject to investigation (e.g., Tormen et al. 1998; Ghigna et al. 1998; Moore et al. 1999; Klypin et al. 1999a,b; Gao et al. 2004a,b; Gnedin et al. 2004; Reed et al. 2005; Diemand et al. 2008; Springel et al. 2008). This includes the tidal disruption of subhalos and their subsequent mixing with the background material. It is expected that even after full tidal dissolution of subhalos, the associated currents (streamers) will persist for a longer time period. Both subhalos and streamers when penetrating the central region can affect the disk evolution in various ways which can be, in principle, observable. Hence, it is important to understand the role of baryons in the subhalo evolution — if baryons can substantially modify the subhalos and their remnants, ultimately this may affect the disk evolution as well.

The effect of baryons on the evolution of the DM substructure was considered recently by Weinberg et al. (2008). They find that the DM dictates the galaxy clustering while the baryons affect the small-scale DM distribution. The fate of the subhalos appears to be most heavily influenced in the denser regions, where the baryons enhance the binding of subhalos. While we defer the comparison between the substructure evolution with and without baryons to Paper II, various aspects of prime halo — substructure interactions are analyzed here as well. We confirm some of the evolutionary trends addressed by Weinberg et al. (2008). Furthermore, due to the superior resolution of our numerical simulations on a galactic scale, e.g., nearly three orders of magnitude in mass resolution, we are able to zoom into specific dynamical processes which accompany the prime halo buildup, the substructure evolution, and halo relaxation processes in the presence of baryons.

While we adopt the current characterization of DM halos in terms of the spherical overdensity, i.e., the NFW profile and the characteristic radius $R_{\rm s}$ for the pure DM simulations, we also attempt to break away from this description in favor of arbitrarily shaped halos. Furthermore, the NFW density profile does not fit the DM distribution in the presence of baryons (e.g., Romano-Diaz et al. 2008c), especially in the inner halo and so we drop this approach altogether.

This paper is structured as follows. §2 deals with numerics, initial conditions and related issues. §3 and §4 present results of numerical simulations and their analysis, and §5 describes the global baryon evolution, while the issues of disk evolution will be discussed elsewhere. Discussion and conclusions follow in §6.

2. NUMERICS AND INITIAL CONDITIONS

Numerical simulations have been performed using the parallel version of FTM-4.5 hybrid N-body/SPH code (e.g., Heller & Shlosman 1994; Heller, Shlosman & Athanassoula 2007). The total number of DM particles is $N \approx 2.2 \times 10^6$ and of the SPH particles is 4×10^5. The gravitational forces are computed using the falcON routine (Dehnen 2002) which is about ten times faster than optimally-coded Barnes & Hut (1986) tree code and and scales as O(N). The tolerance parameter θ was fixed at 0.55. The gravitational softening is $\epsilon = 500$ pc for the DM, stars and gas. The mass density and gravitational potential of the softening kernel are given as (Walter Dehnen, private communication)

$$\rho(r) = \frac{15}{8\pi} \frac{\epsilon^4}{(r^2+\epsilon^2)^{7/2}} \tag{1}$$

$$\Phi(r) = -\frac{G}{\sqrt{r^2+\epsilon^2}} \left[1 + \frac{\epsilon^2}{2(r^2+\epsilon^2)}\right]. \tag{2}$$

The density in eq. 1 falls off faster than a Plummer sphere at large radii, i.e., r^{-7} vs. r^{-5}, which avoids the force bias inherent to Plummer softening (Dehnen 2001).

We use the vacuum boundary conditions and perform simulations with physical coordinates. The cosmological constant is introduced by an explicit term in the acceleration equation. We assume the ΛCDM scenario with WMAP3 parameters: $\Omega_{\rm m} = 0.24$ and $\Omega_\Lambda = 0.76$ and $h = 0.73$, where h is the Hubble constant in units of 100 km s^{-1} Mpc^{-1}. The variance $\sigma_8 = 0.76$ of the density field convolved with the top-hat window of radius $8h^{-1}$ Mpc was used to normalize the power spectrum. The conservation of the total angular momentum and energy within the computational sphere in the PDM simulations has been followed and is within $\sim 0.01\%$ and $\sim 1\%$ respectively. The evolution of various parameters characterizing the DM and baryons has been followed in 1,000 snapshots, linearly spaced in the cosmological expansion parameter a. In these simulations we have switched off the external UV background.

2.1. *Star Formation and Feedback Processes*

We model star formation (SF) processes and associated feedback as described in Heller & Shlosman (1994) and Heller et al. (2007), which should be consulted for details. For SF to occur the local gas must meet several conditions, including being Jeans-unstable. Feedback from OB stellar winds and supernovae (SN) Type II is accounted for by injecting energy from SN and stellar winds into the $N_{\rm SF} = 16$ surrounding gas particles. The

time step of such "active" stellar particles (and of all the gas particles) is restricted in order to properly resolve the feedback timescale. The radiative cooling of $N_{\rm SF}$ gas particles in the vicinity of the "active" stellar particles is temporarily disabled when receiving the energy from a stellar particle. A fraction of this energy is thermalized and deposited in the gas in the form of a thermal energy, then converted to kinetic energy through the equations of motion. This method is preferable over injecting a fraction of the stellar energy directly in the form of a kinetic energy.

The resulting SF rate is that of the Schmidt-Kennicutt law (e.g., Kennicutt 1998) and depends on the adopted fudge factors which determine the stellar energy feedback, $\epsilon_{\rm SF}$ (i.e., the fraction of the thermalized energy), the threshold for the SF as a fraction of the background gas density, $\alpha_{\rm crit}$, and the collapse time of a cloud in terms of the local dynamical time, $\alpha_{\rm ff}$. These factors are fixed at $\epsilon_{\rm SF} = 0.3$, $\alpha_{\rm crit} = 0.5$ and $\alpha_{\rm ff} = 1$ following Heller et al. (2007).

We introduce the probability that a gas particle of mass $m_{\rm g}$ produces a stellar particle of mass $m_{\rm s}$ during a given timestep and multiple generations of stars are allowed to form from each gas particle. A fraction 0.4 of the stellar mass is instantaneously recycled to the parent gas particle. The evolution of gas metallicity is followed and the fraction of massive stars that lead to the OB stellar winds and SN is calculated from the Salpeter IMF.

The thermal balance in the gas is calculated using the energy equation. Adiabatic, viscous and radiative processes are included in the gas heating and cooling. The fractions of H^+, He, He+, He^{++} and e^- are calculated in tandem with the mean molecular weight as a function of density and temperature, assuming optically-thin primordial composition gas.

2.2. *Initial Conditions: Constrained Realizations Method*

We use the method of Constrained Realizations (CRs, Bertschinger 1987; Hoffman & Ribak 1991; van de Weygaert & Bertschinger 1996) and follow the prescription of Hoffman & Ribak (1991) to build the initial conditions within a restricted cubic volume of space with sides $L = 8h^{-1}$Mpc in the ΛCDM cosmology, where a sphere of $5h^{-1}$ Mpc is carved out and evolved from $z = 120$. The constructed Gaussian fields obey a set of constraints of arbitrary amplitudes and positions. The CR algorithm is exact, involves no iterations and is based on the property that the residual of the field from its mean is statistically independent of the actual numerical value of the constraints (see also Romano-Diaz et al. 2006, 2007). This method allows tailoring of the initial conditions to explore how fundamental characteristics of the structure formation history affect the resulting properties of DM and baryons within the computational cube.

A series of linear constraints have been applied on the initial density field. Each of the constraints represents the value of the initial density at various locations and evaluated with different Gaussian smoothing kernels — their width fixed in order to encompass a mass M (the mass scale on which the constraints are imposed). The designed models are based on two constraints. The first one has the mass of $1.0\times10^{12}\ h^{-1}M_\odot$. This implies a $\delta = 3$ overdensity, which constitutes a 2.5σ perturbation and was imposed on a 256^3 grid. It is projected to collapse at $z_{\rm c} \sim 1.3$, based on the top-hat model, and is embedded in a region (2nd constraint) corresponding to the mass of $5 \times 10^{13}\ h^{-1}M_\odot$ in which the over-density is zero, corresponding to the unperturbed universe. The random component in CRs favors formation of similar structures which leads to major mergers.

The total mass inside the computational sphere is $\sim 6.1 \times 10^{12}\ h^{-1}M_\odot$. To introduce the baryons, we have replaced some DM particles on the initial conditions grid by a baryon (i.e., Smooth Particle Hydrodynamics, hereafter SPH) particles, so that $\Omega_{\rm m}$ stays the same for pure DM and baryonic perturbations. The initial masses of DM and SPH particles are the same, 2.78×10^6 $M_\odot$.

3. RESULTS: PDM AND BDM HALOS BUILDUP

3.1. *Primary Halo Characteristic Radii, Radial Density Profiles and Concentrations*

We use the DM mass density peak in order to find the prime halo (by means of the HOP algorithm, Eisenstein & Hut [1998]). The corresponding subhalo finding algorithm is described in Paper II. The subhalo tidal radii are described in §3.6. The density peaks of all three DM and baryonic components may not coincide among themselves. As we follow the buildup of the prime halo, we sample it at characteristic radii defined below. The outermost radius describes the region that has just virialized. Smaller characteristic radii depend more on the density peak properties, where virialization is more complete.

The initial (linear) density field corresponds to a filament running across the computational box and having a 'banana' shape (Fig. 1). The prime halo assembly is shown in Fig. 2. The major mergers epoch ends at $t \sim 4.5$ Gyr, which corresponds to $z \sim 1.5$, in agreement with the prescribed $z_{\rm c}$.

The halo virial radius is defined here in the context of the spherical top-hat collapse model, $M_{\rm vir}= 4/3\pi\Delta(z)\rho(z){R_{\rm vir}}^3$, where $\Delta(z)$ (Bryan & Norman 1998) is the critical overdensity at virialization. It signifies the part of the flow which is virialized, at least partially. As seen in Fig. 2, the outermost spherical surface contains DM mass which by $z = 0$ is about $M_{\rm vir}\sim 3.5 \times 10^{12}\ M_\odot$ (i.e., $\sim 3.9 \times 10^{12}\ M_\odot$ and $\sim 3.2 \times 10^{12}\ M_\odot$, in PDM and BDM models, respectively) and has $R_{\rm vir}\sim$ 400 kpc (i.e., 412 kpc and 385 kpc, respectively). Hence baryons have a minimal impact on the halo overall size and mass in these simulations. During the major merger epoch, $R_{\rm vir}$ in Fig. 2 accurately follows the line of the open triangles which delineates the double of the turnover time, i.e., the collapse time for this mass. At later times, the actual collapse time is slightly longer than the top-hat estimate. Most of the mass shows only mild virial oscillations after they enter $R_{\rm vir}$. We note that $M_{\rm vir}$ curve is an over-estimate during the major merger epoch. $R_{\rm vir}$ of the prime halo and neighboring massive subhalos overlap because of the initial conditions, and the mass of the subhalos is added to the prime halo in this case.

The virial masses of the prime halos in PDM and BDM models grow in tandem most of the time. However, around $z \sim 4$, the PDM halo becomes more massive by a factor of 5 for a brief period of time. We do not attribute any real significance to this event which is related to a slightly shifted merging history.

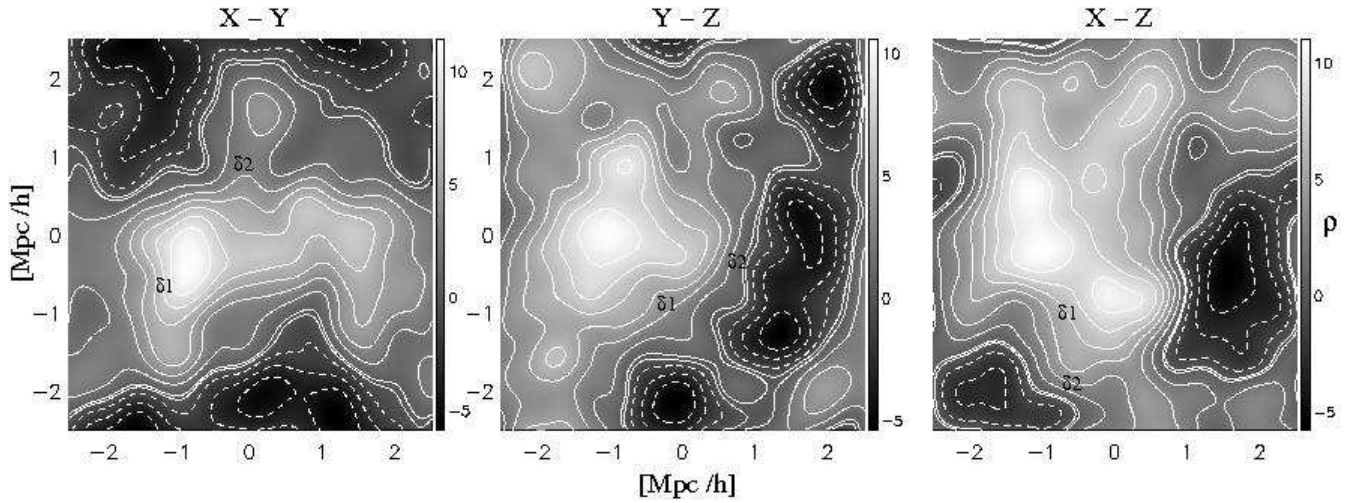

FIG. 1.— Initial conditions: The linear over-density field presented on the three principal planes of the simulation, going through the center of a box of co-moving $5h^{-1}$ Mpc on the side. This field is normalized by its present epoch value and is presented with a Gaussian smoothing on a mass scale of $10^{10}h^{-1}\mathrm{M}_{\odot}$. The thick solid line corresponds to the over-density $\delta = 0$, and solid (dashed) lines correspond to positive (negative) perturbations. The imposed constraints are $\delta_1 = 3.0$ on a mass scale of $M = 10^{12}h^{-1}\mathrm{M}_{\odot}$ and $\delta_2 = 0$ on a mass scale of $M = 5 \times 10^{13}h^{-1}\mathrm{M}_{\odot}$. Both are imposed at the center of the box.

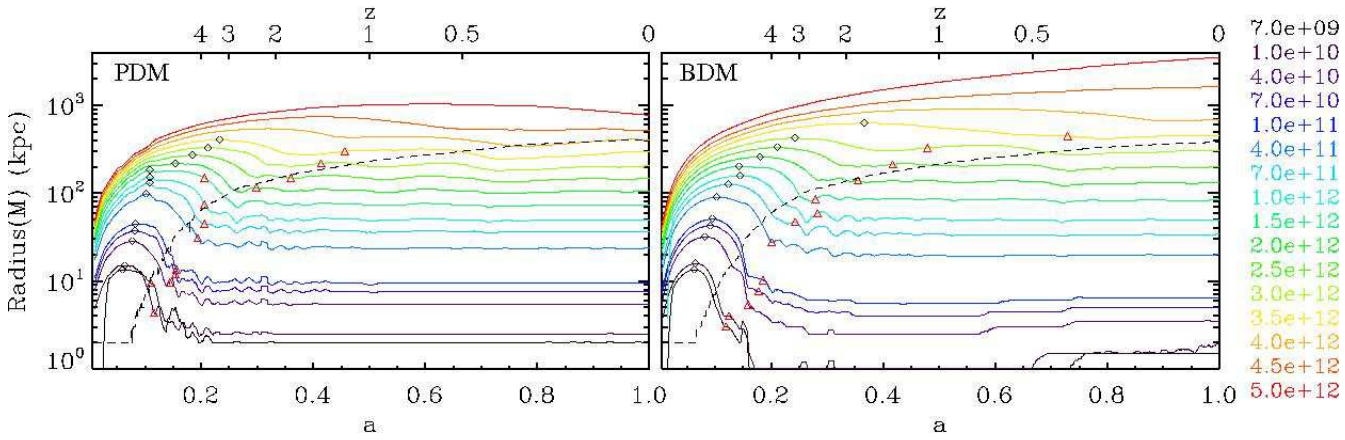

FIG. 2.— DM halo buildup in the PDM (left) and BDM (right) simulations: evolution of radii containing the fixed masses. The dashed lines display $R_{\rm vir}$, open diamonds — the turnover time for each mass, and triangles — the collapse time measured as twice the turnover time. $M_{\rm vir}$ at $z = 0$ are $4 \times 10^{12}M_{\odot}$, and the $R_{\rm vir}$ radii in the PDM and BDM are nearly identical, ~ 400 kpc.

The radial DM density profiles in the PDM model are well fitted by the NFW profile and define the characteristic radius $R_{\rm s}$ where the $\log\rho - \log R$ slope is –2. A comparison between the PDM and BDM halo density profiles reveal substantial evolutionary differences, even in the early stages, at $z \sim 5$. At low z, the DM density profiles are similar outside $\sim$ 20 kpc, the PDM profile being slightly higher than the BDM one (Romano-Diaz et al. 2008b). Inside this radius, the BDM density profile is steeper and takes over. Romano-Diaz et al. (2008b) have analyzed the evolution of this region and shown that after $z \sim 4$ the DM in the BDM acquires the slope of an isothermal distribution, -2, in $\log\rho - \log R$ within the central $\sim$ 15 kpc — the result of an adiabatic contraction. This *isothermal* cusp is gradually leveled off after $z \sim 1$ by the heating action of accreting subhalos. The flat core forms within the inner $2 - 3$ kpc. We do not pursue this issue further here and only comment that the flattening of the isothermal cusp cannot be related to the finite resolution of the code as it produces less than 5% difference between the gravitationally softened force and the exact Newtonian force of point masses at 1 kpc from the center. Hence, the BDM density profile cannot be fitted by the NFW profile around $R_{\rm s}$ and at smaller radii. We, therefore, define an alternative radius which samples this region.

The radius of a maximal circular velocity, $R_{\rm vmax}$, in the DM halo has a universal character when the NFW fit is used, and

$$\gamma \equiv \frac{R_{\rm s}}{R_{\rm vmax}} \sim 0.46. \qquad (3)$$

This radius provides a robust sampling of inner halo properties. We define a characteristic radius $\tilde{R}_{\rm s}$ which is a constant fraction $\gamma = 0.46$ of $R_{\rm vmax}$ and apply it instead of $R_{\rm s}$ to the BDM and PDM models. In the latter case, $\tilde{R}_{\rm s} \equiv R_{\rm s}$, by definition. The three radii, $R_{\rm vir}$, $R_{\rm vmax}$ and $\tilde{R}_{\rm s}$ are utilized by us to sample the outer and inner

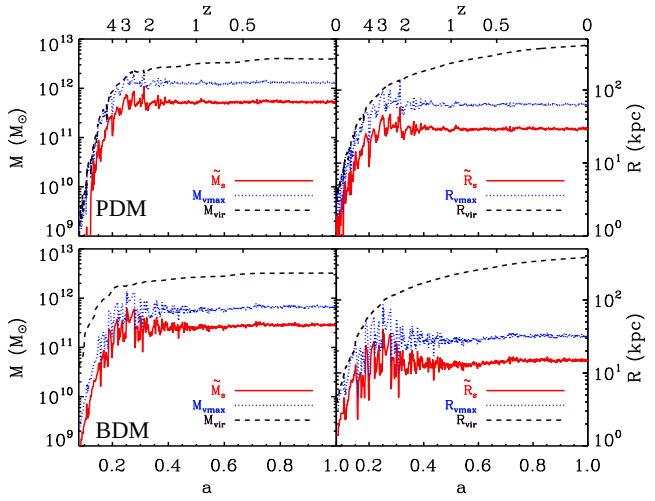

FIG. 3.— Evolution of the characteristic masses (in $M_\odot$) and radii (kpc) for the prime halo in PDM (upper) and BDM (lower) models. $\tilde{M}_s$ and $\tilde{R}_s$ (red), M_{vmax} and R_{vmax} (blue), and M_{vir} and R_{vir} (black).

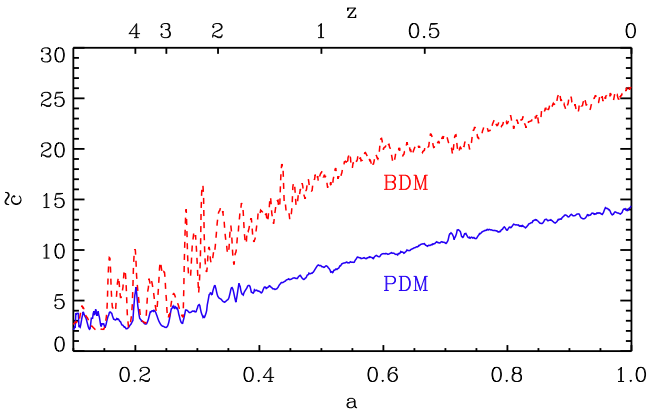

FIG. 4.— Evolution of the concentration paramater $\tilde{c}$ in PDM and BDM models.

halos. Quantities defined at $\tilde{R}_s$ will bear *tilde*.

The final $\tilde{R}_s$ reach $\sim$ 28 kpc and $\sim$ 15 kpc, while R_{vmax} becomes 62 kpc and 32 kpc, in PDM and BDM, respectively. The growth of $\tilde{R}_s$ and R_{vmax} is essentially terminated after the epoch of major mergers, but R_{vir} continues to grow albeit at a slower pace (Fig. 3). This agrees well with earlier results (e.g., Wechsler et al. 2002, Romano-Diaz et al. 2006, 2007; Diemand, Kuhlen & Madau 2007). We note that quantities defined within $\tilde{R}_s$ and R_{vmax} typically show a very similar temporal behavior, e.g., the mass within these radii.

The concentration parameter, $\tilde{c} \equiv R_{vir}/\tilde{R}_s$, reveals the differences in the evolution of the outer and inner halos. It shows a substantial departure of PDM from the BDM model (Fig. 4). The source of this difference is the adiabatic contraction of the DM which results in a more concentrated halo.

Determining the halo's center-of-mass (CoM) is not trivial, especially when baryons are present in the form of stars and gas, in addition to the DM. The main complication comes from the assembling halo being an open

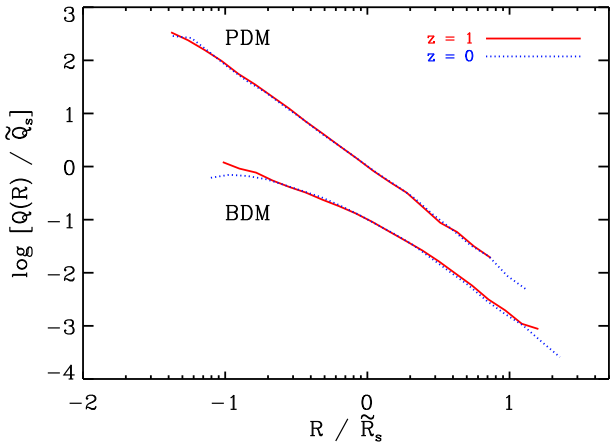

FIG. 5.— The DM phase-space density, $Q(R)$ for PDM and BDM halos. The x-axis was normalized by $\tilde{R}_s$ at $z = 1$ and 0, and y-axis by the value of Q at $\tilde{R}_s$, $\tilde{Q}_s$, at these z. The BDM curves are displaced by 0.1 vertically down for clarity.

system, both during the quiescent accretion and major merger phases. The CoM normally does not coincide with the density peak. Moreover, the density peaks of all three DM and baryonic components may not coincide among themselves, especially because the halo is not fully relaxed and is found only in a rough virial equilibrium. During a merger event, the position of the halo CoM jumps nearly discontinuously, when R_{vir} is penetrated, but dynamics of the cold baryons (i.e., the disk) which are assembled within the central 10 kpc – 20 kpc is unaffected, unless there is a direct intrusion into this central region before the intruder is largely dissolved. In this latter case the disk dynamics is affected dramatically. As we shall see, this is not limited to the merger epoch only, and is important during the subhalos influx after $z \sim 1$ as well.

3.2. *Primary Halo in the Phase-Space*

We have compared the phase-space density, $Q(R)$ in the PDM and BDM halos (Fig. 5). While we confirm that for the PDM it can be fitted by the power law $Q(R) = \tilde{Q}_s(R/R_s)^{-\beta}$, with $\tilde{Q}_s \equiv \tilde{\rho}_s/\tilde{\sigma}_s^3$, where $\tilde{\sigma}_s$ is the 1-D radial DM dispersion velocity at $\tilde{R}_s$ and $\beta \sim 1.95$ in the quiescent epoch (e.g., Hoffman et al. (2007). This dispersion velocity has been calculated using the SPH kernel with 64 neighbors. However, the BDM halo cannot be fit by this law after $z \sim 4$. The difference between the models is most visible within the central $\sim$ 30 kpc, where the BDM $Q(R)$ starts to flatten. This process accelerates after $z \sim 0.5$, when Q develops a flat core within the central few kpc.

3.3. *Primary Halo Shapes*

We follow Heller et al. (2007) in calculating the DM halo shapes. After substracting the halo COM velocity, we compute the eigenvalues of the moment of inertia tensor for the DM mass within a specified radius. Next, we determine the semi-axes $a > b > c$ of a uniform spheroid using these eigenvalues. The axes ratios are used to characterize the halo shapes as defined by $b/a = \sqrt{(e_1 - e_2 + e_3)/\Delta}$, and $c/a =$

$\sqrt{(e_1+e_2-e_3)/\Delta}$, where $\Delta = e_2 - e_1 + e_3$ for the eigenvalues $e_3 > e_2 > e_1$. The axial ratios have been computed in two ways, as a function of time and as a function of R. In the former case, we calculate an integral value of b/a and c/a which represents the entire DM within $R_{\rm vir}$. In the latter case, we use the DM shells and look at the radial distribution of their axial ratios.

We confirm that the baryons do have a substantial effect on the halo axial ratios, after a detailed comparison as shown by Dubinski (1994), Kazantzidis et al. (2004) and Berentzen & Shlosman (2006). The ratios b/a and c/a are decreasing until the end of the major merger epoch at $a \sim 0.4$, except for b/a of the inner layers in the BDM halo. Thereafter, the halos experience a gradual decrease in their equatorial ellipticity, $\epsilon_\rho = 1 - b/a$, and flatness, $f_\rho = 1 - c/a$, with time, at all radii. For the outer radii, this trend is more obvious and the *gradient* of triaxiality is slowly erased, but the outer layers remain always more triaxial. This is more or less in line with Heller et al. (2007). At $z = 0$, the globally averaged axial ratios are $b/a \sim 0.8 - 0.9$ and $c/a \sim 0.7 - 0.8$ for the PDM model. For the BDM, these ratios are larger, $b/a \sim 0.9 - 0.95$ and $c/a \sim 0.8 - 0.9$ at the end. The same trend is observed for the radial profiles of the axial ratios. The halos appear slightly more elliptical at the intermediate radii and nearly axisymmetric in the central 10 kpc. The c/a seems to be independent of r, except in the central 10 kpc where it tends to unity.

To summarize, while the outer layers of PDM and BDM halos evolve in a similar fashion, i.e., become more triaxial during the major merger epoch, and less triaxial during the subsequent smooth accretion permeated by minor mergers, the inner layer of the BDM halo starts to lose its ϵ_ρ early, after the initial collapse. The outer halos appear prolate at all times, while inner halos are nearly oblate at lower z. We note, that while relative differences between the PDM and BDM simulations appear robust, they must be tested also against halos with different merger histories.

3.4. *Primary Halo Figure Tumbling and Angular Momentum*

Calculating the halo shape (§3.3) and following the orientation of the halo major axis, we find that the halo figures in PDM and BDM simulations are essentially nonrotating (Fig. 6), based on the temporal resolution of $\sim$ 900 snapshots. Rather the halos librate around a fixed direction by $\pm 10°$. Our dense temporal coverage allows the disentanglement of the effects of moving substructures (e.g., subhalos and tidal streams) which can otherwise introduce aliases and result in erroneous estimates for the halo figure rotation. After the epoch of the major mergers, and especially toward the end of the simulations, the triaxiality gradients between the inner and outer halo shells are substantially diminished, hence the effect of the outer shells on the overall shape is not so pronounced.

The difference between the exceedingly slow halo tumbling found in the previous models and the non-tumbling halos in the present simulations is *dynamically* unimportant. In the current models, the orientation of the halo major axis is nearly fixed in time with respect to the orientation of the main DM filament — the consequence of gravitational torques from the filament which is able to focus the smooth and clumpy accretion onto the halos. While the torque on the filament itself from the large-scale structure is ignored here, if this torque is passed onto the halo, the resulting halo tumbling will be still dynamically insignificant.

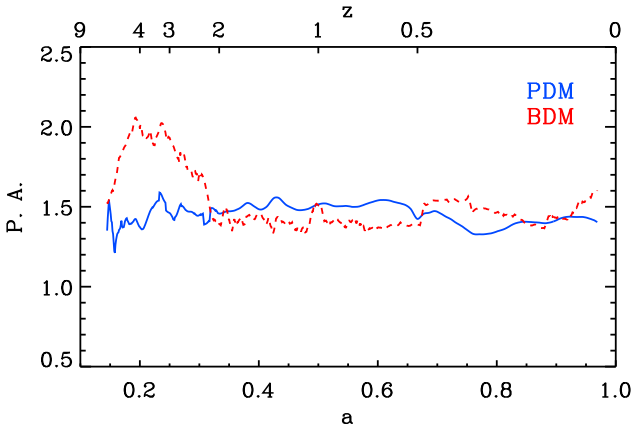

FIG. 6.— The position angle (P.A., in radians) of the major axis of DM halo in PDM (solid, blue) and BDM (dashed, red) models. Based on $\sim$ 900 snapshots.

While the prime halo axes librate around a preferred direction, its internal circulation angular momentum shows much more evolution. Here we refer to the momenta of DM, unless stated otherwise, and define the total, J, and specific, j, angular momenta within three characteristic radii of the prime halos, with respect to their CoM. The correlations between J of baryons and DM are discussed in §5.

Both $\tilde{J}_{\rm s}$ and $\tilde{j}_{\rm s}$ end up substantially higher in BDM than in PDM model, by a factor of $\sim$ 5 — a possible signature of disk angular momentum transfer to the inner halo. This is observed despite that $\tilde{R}_{\rm s}$ in BDM samples a smaller region than in PDM. Moreover, $\tilde{J}_{\rm s}$ and $\tilde{j}_{\rm s}$ in BDM are nearly constant with time while those in PDM are variable and show a decline toward $z = 0$. We have tested the radial distribution of $j(M)$, where $M(R)$ is the DM mass within R. At $z = 0$, $j(M) \sim M^s$ and $s \sim 0.91$ and ~ 0.96, in the PDM and BDM halos, respectively. This lies within the acceptable range for s in the statistical study j distribution of Bullock et al. (2001, see their Fig. 16).

While the values of $J_{\rm vir}$ in both models do not change by more than a factor of $\sim 2-3$ after the major mergers, the orientation of $\vec{\mathbf{J}}_{\rm vir}$ changes with the characteristic timescale of $\sim 1-2$ Gyr by 'flip-floping' $\sim \pi - 2\pi$ angle. These events are not limited to the major merger epoch. This effect has been already noted by Porciani, Dekel & Hoffman (2002)

3.5. *Energy Constraint on Radial Motion in DM Halos*

For the 'collisionless' particle motions in galaxies, the mean free path is much larger than the size of the system. However, such particle motions are usually limited by energy and angular momentum considerations, or by their combination. We start with the simplest question. How does the energy consideration limit the particle motions in a halo whose figure rotation is negligible?

In both models presented here, about $4 \times 10^{12}\ M_\odot$ of the halo have collapsed by $z = 0$ and the oscillations have been quickly damped (Fig. 2). In §4, we show that the virialized part of the halo is dominated by the DM currents, is clumpy and not fully stratified. In view of this, we ask the following question: what fraction of particles found within R at time t is confined within this radius? Specifically, is the mass within each spherical surface R made up of predominantly localized (i.e., locally bound) particles or freely streaming particles across this boundary?

The motion of halo particles has corollaries for the disk-halo interaction and angular momentum exchange and we pursue this elsewhere. Here we attempt to develop a number of indicators which *quantify* the dynamical state of the halo during and following the merger epoch.

We first estimate the fraction of the bound particles, $\eta(R)$, within R as a function of z in the PDM and BDM prime halos by counting the number of particles with a total energy below some (negative) value. Because the halos are non-spherical, this value corresponds to three different radii along the halo principal axes — the smallest radius is used here. The bound fraction within R is obtained by dividing the number of bound particles by the total number of particles within this R at a particular moment of time.

For a comparison, we use the non-singular isothermal sphere. The total mass of the NSIS is about 20% higher than $M_{\rm vir}$ at $z = 0$. The NSIS is created close to equilibrium and is allowed to relax.

We present the radial distributions of the fraction of bound particles in the halos and in the NSIS, at various z. The radii are normalized by $R_{\rm vmax}$ in all cases for a direct comparison. The fraction of bound particles in the models increases with time at high z, but stays remarkably constant after the epoch of major mergers, $z \lesssim 2$ (Fig. 7). At later times, η is relatively flat with R, except within $\tilde{R}_{\rm s}$. It is about 11% and 15% at $\tilde{R}_{\rm s}$, 17% and 23% at $R_{\rm vmax}$, and 43% and 57% at $R_{\rm vir}$, for PDM and BDM respectively. Closer to the center, within the NFW cusp region, η falls dramatically below 1%.

The bound fractions within the PDM and BDM models and the NSIS agree nicely at large radii. Within $R_{\rm vmax}$, however, the BDM halo is more bound, especially at $z \gtrsim 1$ when its $\rho_{\rm DM} \sim R^{-2}$ because of the adiabatic contraction. Even the PDM is more bound here than NSIS. However, closer in, within the cusp region, the flat core of the BDM is less bound than the NSIS and especially of the PDM. Consequently, one should expect relatively larger radial excursions of the NSIS particles throughout $R_{\rm vmax}$ compared to the PDM and BDM. Within the flat core, the BDM particles will exhibit the larger radial excursions.

Overall, the energy consideration in the halo provides a very weak constraint on the DM particles motions — a large fraction of particles are not bound within a particular halo region but exersize large radial motions. The next question is whether these motions correspond to a coherent behavior of a large number of particles. We attempt to answer this question in §4.

We find that about 50%, 20% and 13% of DM particles in PDM and BDM models within $R_{\rm vir}$, $R_{\rm vmax}$ and $\tilde{R}_{\rm s}$, respectively, are bound at $z = 0$. Fig. 8 shows that these

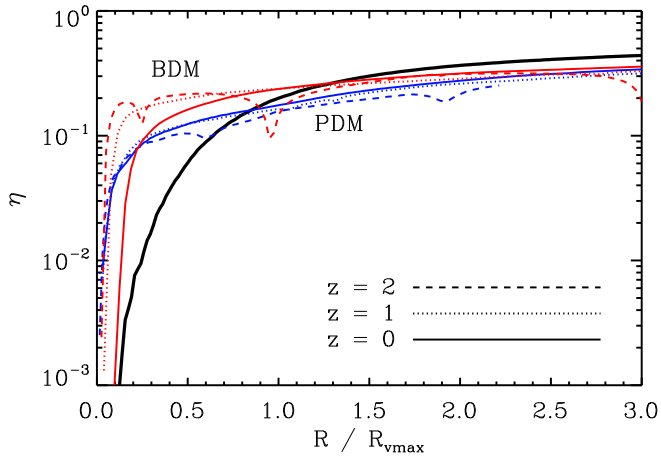

FIG. 7.— Bound fractions of DM, $\eta(R)$, in the prime halo of the PDM (blue) and BDM (red) models and in the non-singular isothermal sphere, NSIS (thick black). All radii are normalized by $R_{\rm vmax}$, for a direct comparison. The lines correspond to $z = 2$ (dashed), $z = 1$ (dot-dashed) and $z = 0$ (thin solid). The wiggles at higher z are due to the presence of subhalos.

bound fractions, η, are nearly constant with time within $R_{\rm vmax}$ and $\tilde{R}_{\rm s}$, except the fraction within $\tilde{R}_{\rm s}$ in the BDM which declines slowly. The bound fractions within $R_{\rm vir}$ show a secular growth which mirrors that of the $M_{\rm vir}$ itself.

We also confirm that the *bound* DM mass within $\tilde{R}_{\rm s}$ assemble by the end of the merger period (e.g., Wechsler et al. 2002), as well as for $R_{\rm vmax}$. However, as exhibited by Fig. 8, these fractions within $\tilde{R}_{\rm s}$ and $R_{\rm vmax}$ are small and most of the mass is contributed by the locally unbound particles. Therefore, one cannot conclude that the mass accumulation within these radii terminates with the major mergers.

3.6. *Subhalos Contribution to the Prime Halo Buildup*

While the evolution of the subhalo population is addressed in the companion Paper II, here we estimate its contribution to the buildup of the prime halo mass within $\tilde{R}_{\rm s}$, $R_{\rm vmax}$ and $R_{\rm vir}$. We are not only interested in the contribution by the major mergers, i.e., mergers with the mass ratios $\gtrsim 1:3$, but also smaller ratios of $\gtrsim 1:10$ and down to $\sim 10^{-4}$, which we (arbitrary) consider as the limit of clumpy accretion. This corresponds to the subhalo mass of $4 \times 10^8\ M_\odot$, which is still well resolved in our simulations. Any accreted clump below this value is considered a part of a smooth accretion. We also analyze the history of DM particles bound within the characteristic radii.

We briefly outline our two methods of calculating the merger mass ratios. The subhalo mass is calculated after determining its tidal radius. In the first method, we determine the tidal radii using the spherical overdensities of the prime halo and subhalos crossing $R_{\rm vir}$ of the prime. We associate redshift $z_{\rm touch}$ with subhalos entering this radius. The second method is based on the prime halo and subhalos density isocontours and does not involve sphericalization. We determine the 3-D isodensity contours and define the 'virial' contour $\rho_{\rm vir} \equiv \Delta(z)\rho_{\rm crit}$ as the halo boundary. The subhalo mass is taken as its

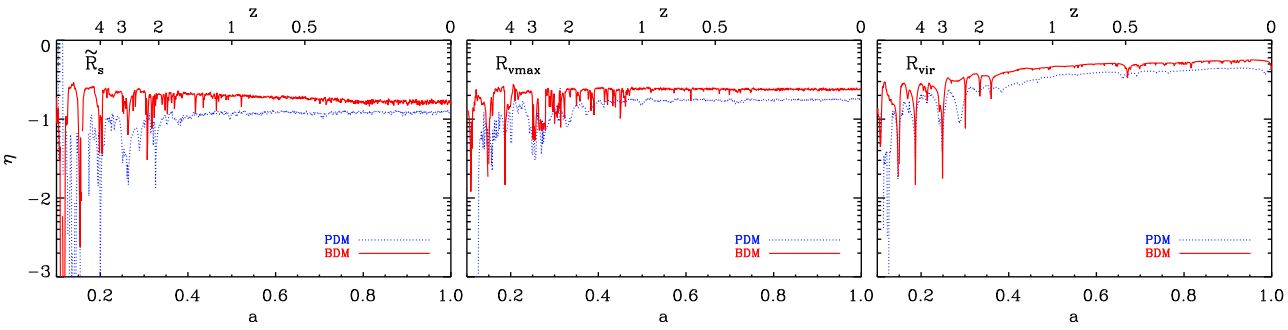

FIG. 8.— Evolution of bound DM fractions, η, in PDM and BDM models within $\tilde{R}_s$ (left), R_{vmax} (middle) and R_{vir} (right).

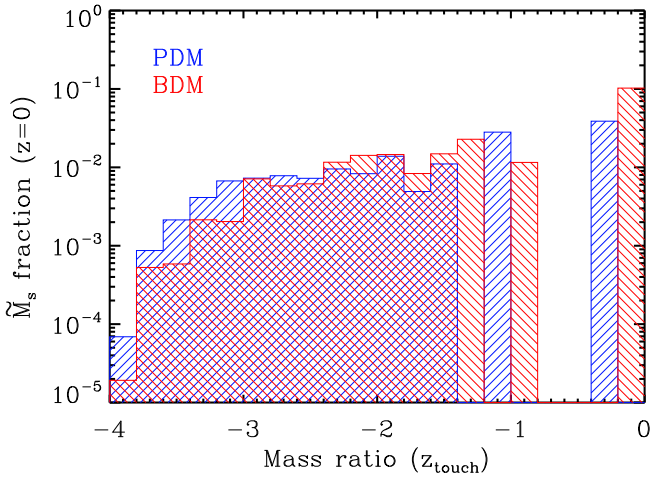

FIG. 9.— Fraction of the subhalo population mass residing within $\tilde{R}_s$ at $z = 0$ in the PDM (blue) and BDM (red) models as a function of the merger mass ratio (subhalo-to-prime halo, see text) calculated at 'touching' z_{touch}. DM accreted with mass ratios less than 10^{-4} is accounted for as a smooth accretion. This value corresponds to a subhalo of 4×10^8 $M_\odot$, well resolved in these simulations.

tidally-truncated value when it crosses ρ_{vir}. In this paper we use the latter definition of merger mass ratios and compare it with the former one in Paper II.

About 15% and 33% of $\tilde{M}_s$ (the DM only mass in PDM and BDM) contributed by subhalos is found within $\tilde{R}_s$ of the prime halos at $z = 0$, respectively (Fig. 9). That includes 4% and 20% from the major mergers, and 11% and 15%, respectively, from the minor mergers. The rest came from the smooth accretion. Overall, contribution to M_s and $\tilde{M}_s$ from mergers, when counted per decade of the mass ratio, falls off slowly (Fig. 9), from 1:1 to 10^{-3}. Lower mass ratio mergers contribute little to the central mass, but the total contribution from smooth (unresolved) accretion dominates.

4. RESULTS: KINEMATICS OF DM BUILDUP IN PDM AND BDM MODELS

Hydrostatic equilibrium refers to an internal state when the inward force of gravity is balanced by the pressure gradient force. The fluid element must also be at rest, so no large-scale motions are allowed. The latter condition is not strickly fulfilled in the halo which forms within the hierarchical merging scenario. The pressure gradient term in collisionless systems is given by the gradient of a stress tensor, whose off-diagonal terms are comparable in magnitude to the diagonal ones and are responsible for the non-conservation of circulation. Therefore, in collisionless systems these terms drive evolution on much shorter dynamical timescales than in fluids, where the off-diagonal terms are small because they represent viscous forces (Christodoulou et al. 1995).

The drive of the DM halos towards the virial equilibrium is accompanied by the violent relaxation (Lynden-Bell 1967). However the efficiency of violent relaxation depends dramatically on the presence of residual currents in the halo, in liu of the quickly decaying central potential oscillations. Such currents are in fact favored in our simulations because of the presence of large-scale filaments, as they are the natural outcome of cosmological initial conditions. The main and secondary filaments (e.g., Fig. 1) form at high z. We therefore study the kinematics of these currents and analyze the mixing they introduce in the halo.

The filaments consist of subhalos and a less clumpy material that penetrate R_{vir}, preserve their identity for at least one crossing time (depending on their impact parameter with the main halo) and display dispersion velocities which are substantially lower than in the surrounding halo. In fact, we observe that the 'cold' filament-driven influx is de-focused after passing the pericenter of its motion. As its constituents move out, their slowdown in tandem with the tidal disruption lead to the formation of shells that persist for a long time. Shells that form later in time have larger outflow velocities and can cross shells that formed earlier (Paper II). For the survival of these shells it is important that they form after subhalos pass the pericenters of their orbits.

When discussing the main halo buildup, we distinguish between the first-time entering material and the recycled material. The latter consists of shells, tidal tails and captured subhalos. In the following we continue to abbreviate the spherical components with R and v_R (i.e., particle velocity along R), and cylindrical components with r and v_ϕ (the radius and azimuthal velocity in an arbitrary xy-plane whose origin lies at the DM CoM). In order to specify the kinematics of the buildup, we analyze the $R - v_R$ (in §4.1) and $r - v_\phi$ (in §4.2) diagrams within the inner 300 kpc and zoom into the innermost 20 kpc when focusing on the disk buildup.

4.1. *Halo Evolution in $R - v_{\rm R}$ Plane*

We now follow the evolution of DM particles in the $R-v_{\rm R}$ plane. This reveals the intricacies of halo relaxation beyond virialization — to what extent it 'forgets' the initial conditions and how the substructure is gradually erased. Most importantly, it allows the comparison of the DM kinematics.

The radial velocity field of the DM is dominated by an outflow initially (i.e., cosmological expansion), which slows down from inside-out, reflecting the gradual increase in the turnover radius. Within $R_{\rm vir}$, the distribution of $v_{\rm R}$'s is initially slightly asymmetric with respect to the $v_{\rm R} = 0$ line (Fig. 10 and the Animation Sequence), then gradually decreasing its bias by $z \sim 6$, with the negative $v_{\rm R}$ asymmetry remaining only outside $R_{\rm vir}$. The growth of substructure is clearly visible as local (vertical) distortions in the velocity fields. As the subhalos themselves virialize, these vertical distortions provide information about their binding energies and mutual interactions and mergers. The symmetry of each subhalo peak indicates whether they continue to grow — the more symmetric is the peak with respect to their local CoM, the smaller is their growth rate at this moment.

The epoch of major mergers can be easily followed in Fig. 10. By $z \sim 4$, the $v_{\rm R}$ field is symmetric (with respect to $v = 0$ line) only within the central 60–70 kpc, and even this is a very approximate statement because the substructure is far from being erased there. The main halo buildup can be closely followed — the steady stream of virialized subhalos and the smooth (i.e., below our self-imposed limit) accretion inflow can be clearly distinguished. Outside the growing halo, within some distance, the prevailing velocities are negative, both in smooth and clumpy accretion, with only more massive subhalos contributing to the positive $v_{\rm R}$ (due to the internal velocity dispersions). The major mergers appear as negative $v_{\rm R}$ moving features, then switching to a positive $v_{\rm R}$ at pericenters, producing strong asymmetries.

The destruction of subhalos in tidal interactions and mergers is visible when the vertical velocity feature (spike) of each subhalo inclines clockwise. This corresponds to the formation of tidal tails whose $R - v_{\rm R}$ correlations in particle number density are naturally reproduced and are visible as 'fingers. '

Comparison between different frames in Fig. 10 displays the diverging evolution of the DM in the simulations. The early evolution is very similar in both models, but after $z \sim 4$, both the main halo and the penetrated subhalos increasingly differ. The BDM simulation achieves higher central velocities because of the presence of baryons which drag the DM inwards in an adiabatic contraction. The tidal disruption of subhalos is associated with much more pronounced tidal tails in the BDM, i.e., inclined 'fingers.' The fingers appear longer by a factor of 2 in the BDM.

At higher z, the influx across $R_{\rm vir}$ dominates the buildup, while at lower z's the trapped subhalos and smooth accretion are recycled. Some of the subhalos survive a few orbits (vertical fingers), while other are tidally disrupted (inclined fingers). The recycled part of the accreted material has a longer 'memory at later times — the individual shells survive longer and are less mixed.

The BDM halo becomes substantially more concentrated than the prime halos in the PDM. Note the almost double spread along the $v_{\rm R}$-axis in the former. Moreover, the (inner) shape of the denser (in color) region is smashed against the $v_{\rm R}$-axis in the BDM and has a convex shape in the latter. This difference is explained in terms of the shape of the gravitational potential within the central region of the prime halo.

By $z \sim 3.5$, the radial velocities are symmetric with respect to $v_{\rm R} = 0$ within about the central 100 kpc. This region increases to ~ 200 kpc by $z \sim 2.5$. By $z \sim 2$, the correlation fingers extend well beyond the halo radius, to $R \sim 300$ kpc, beyond 400 kpc at $z \sim 1.7$, beyond 600 kpc at $z \sim 1.4$, and beyond 800 kpc at $z \sim 1$. The outflowing material crosses the 1 Mpc radius by $z \sim 0.8$. The width of the inflowing stream declines with time, while that of the rebounding material increases. The shell structure is easily distinguished in the outflowing material and can be traced across the $v_{\rm R} = 0$ line. Material can be followed in its circulation along these shells up to about 800 kpc at $z \sim 0$, well outside $R_{\rm vir}$.

The 'cold' stream of incoming subhalos and smooth accretion become less dominant by $z \sim 2$ and the $R - v_{\rm R}$ diagram is dominated by the shell structure, but the stream is notiseable even at $z = 0$ where it is the main source of the remaining $v_{\rm R}$ asymmetry within the main halo. Moreover, the $R - v_{\rm R}$ diagram reveals the absence of large virial velocities in the central few kpc, except at a few limited moments when subhalos are passing (or merging) through the center. This is only a characteristic of the pure DM simulations, with the baryonic simulations showing large velocities near the center. As stated above, this difference is caused by a much larger central mass concentration in the latter models.

Lastly, for $z \lesssim 1.5$, three types of motion can be detected in the $R - v_{\rm R}$ plane. The first one corresponds to the clumpy and smooth accretion onto the main halo. This flow dominates the bottom parts of these diagrams at negative velocities. The top part of the diagrams, at positive velocities, represents the outflows of the material processed by the central halo. Initially, it is dominated by fingers of tidally disrupted subhalos, and at later times it is dominated by the shells of the ouflowing material. At progressively lower redshifts those flow out faster because they originate at larger distances from the halo and their infalling velocities increase as well. This causes finger and shell crossings, observable in the diagrams. The mid part of the diagrams is populated by circulating flows which do not escape $R_{\rm vir}$, but show the same finger and shell structure.

As we have seen, the halo while virialized is far from being relaxed. We distinguish three types of substructure corresponding to three consequtive levels of relaxation: the subhalos, the subhalos with tidal tails, and streamers. The subhalos are bound within their tidal radii, while those with tails are clearly found in the process of being tidally disrupted. The streamers are recognizable patterns in the $R - v_{\rm R}$ plane which are not bound but show correlation in this plane. They are expected to be mixed with the background in a few crossing times.

To quantify the degree of relaxation in the main halo, we have subtracted the smoothed version of the halo in the $R-v_{\rm R}$ plane from the original frame. The smoothing kernel is about 15 kpc along the R-axis and 75 km s^{-1} along the $v_{\rm R}$-axis, and the smoothing procedure is mass-

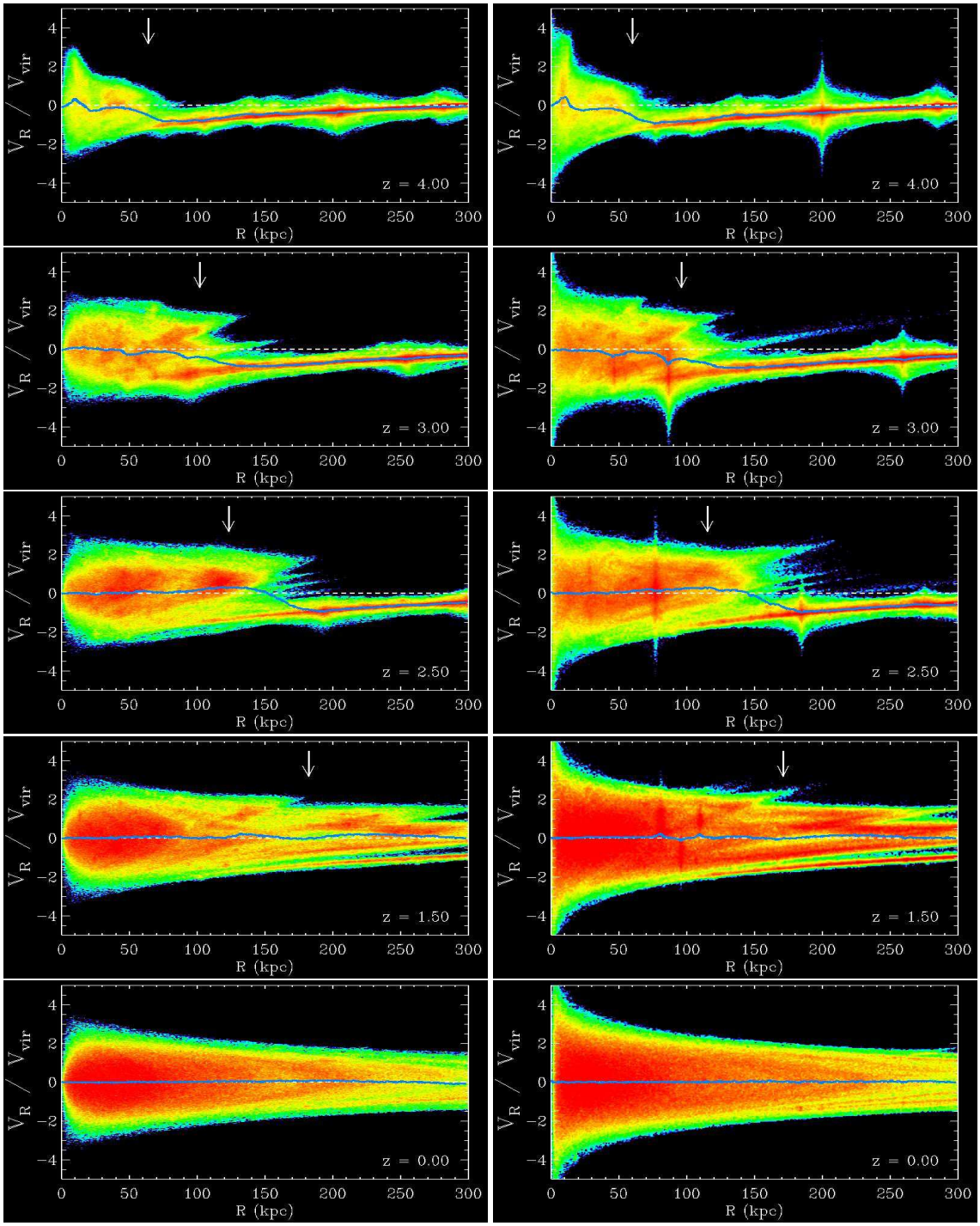

FIG. 10.— Evolution of the DM halo in the PDM (left) and BDM (right) models shown in the $R - v_{\rm R}$ plane at following times: $z = 4$ and 3 (the major merger epoch and the appearance of 'fingers,' and the subsequent minor mergers), and $z = 2.5, 1, 5$ and 0 (the appearance of the shell structure inside and outside of the main halo). The colors correspond to the DM particle density on the $R - v_{\rm R}$ surface. The vertical arrow shows $R_{\rm vir}$, the dashed white line — $v_{\rm R} = 0$, and blue line — the average v_R at each R. The velocity axis is normalized by $v_{\rm vir}$ — the circular velocity at $R_{\rm vir}$. The associated Animation displays the evolution in this plane from $z = 25$ to $z = 0$.

conserving. By subtracting the smoothed image from the original one we get the residual map. We integrate the mass associated with the residuals to obtain the *excess* mass (i.e., over the smoothed halo) associated with the substructure within $R_{\rm vir}$. This procedure allows us to estimate the contribution of the excess DM mass fraction associated with density enhancements (i.e., subhalos, tidal tails and streamers) above some smoothed reference density which is time-adjusted. Fig. 11 shows the evolution of this fractional excess mass. We observe two trends: the excess mass fraction in the substructure becomes more prominent with time and it is marginally

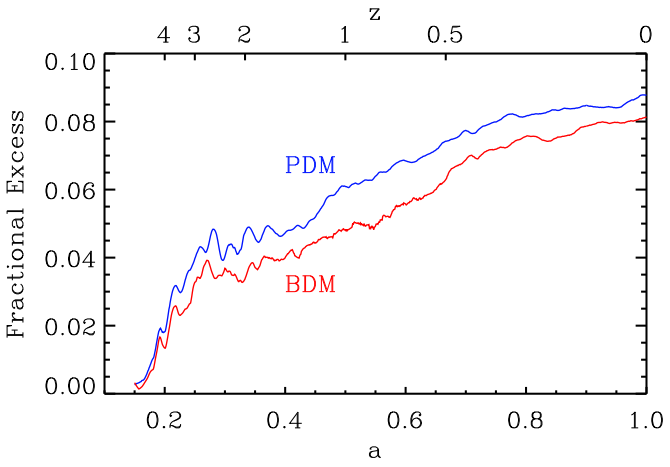

FIG. 11.— Evolution of the *excess* fraction of DM mass associated with substructure, i.e., with subhalos, tidal tails and streamers, in PDM and BDM models. This fraction is calculated by normalizing the residual mass within $R_{\rm vir}$ (e.g., Fig. 10) by $M_{\rm vir}$.

larger in the PDM model. In Paper II we show that the small excess associated with the PDM model originates outside the inner ~ 100 kpc virialized region.

Despite some differences in the definition of subhalos, we compare our results with those of the Aquarius simulation (Springel et al. 2008). The latter arrive at $\sim 11\%$ contribution from subhalo mass within the prime halo $R_{\rm vir}$ at $z = 0$. Fig. 11 shows about $8\% - 9\%$ contribution in our PDM and BDM models at the same time.

4.2. *Halo Evolution in $r - v_\phi$ Plane*

Snapshots of tangential velocities of DM particles are shown in Fig. 12. During the initial expansion these velocities 'cool' down. This distribution is symmetric with respect to $v_\phi = 0$ up to $z \sim 9 - 10$, when the growth of the inhomogeneities feeds v_ϕ with positive or negative asymmetries at small r, during the major mergers epoch. While each major merger forces positive or negative asymmetry at the center, the velocities relax to a symmetric distribution thereafter. Not only major, but also minor mergers can be easily traced in this diagram. By $z \sim 2.5$, this diagram achieves a higher degree of symmetry which is only perturbed by merger events. The v_ϕ distribution widens with r when entering the virialized halo radius. The high degree of symmetry between the number of prograde and retrograde circulating particles is very important in order to understand the dynamical state of the DM halo as well as its ability to interact with the baryonic matter at its center.

The white lines in Fig. 12 correspond to the circular velocities in the main halo as a function of r and are calculated for a spherically-symmetrised halo at z. The halo is substantilly triaxial at all radii and the shown circular velocities provide a bad approximation to the local velocity field in that they underestimate velocities within $R_{\rm vir}$ and overestimate them outside. The overall symmetry in the $r - v_\phi$ diagram confirms that there is very little net circulation of the DM within the halo. We also noted that the halo figure does not tumble and is oriented along the main filament which feeds its growth over the Hubble time.

The first time entering subhalos inside $R_{\rm vir}$ move close to the $v_\phi = 0$ line, as they follow the cold stream from one of the filaments and have a very low angular momentum with respect to the prime halo. Only at small r their v_ϕ become appreciable.

Residual maps in the $r - v_\phi$ plane constructed from Fig. 12 snapshots along the lines outlined above provide very similar results on the estimated mass fraction in the substructure (Fig. 11), and we avoid from displaying it here.

4.3. *Halo Evolution: Dispersion Velocities*

The evolution of DM in the presence of baryons differs in the dispersion velocity map. These differences become visible with the formation of first bound condensations (Fig. 13). The subhalos are much more bound and their internal dispersion velocities reflect this clearly (e.g., spikes). The low velocity dispersions, ~ 10 km s^{-1}, describe the conditions inside the filaments penetrating the halos. The subhalos in the filaments also exhibit low internal velocities. As the inflow penetrates to smaller R, the smaller clumps are obliterated. At higher z, the clumpy nature of the inflow is still visible, but at low z becomes much less obvious.

Next, dispersion velocities display a divergent behavior in the center, $R \lesssim 20$ kpc. While they peak in the BDM, they decline in the PDM (see also Romano-Diaz et al. 2008b). The turnover radius corresponds to $\tilde{R}_{\rm s}$ in the BDM model.

5. RESULTS: KINEMATICS OF BARYON BUILDUP

Baryon influx within $R_{\rm vir}$ proceeds along the filaments and is clumpy (Paper II). The gas temperature gradients become visible at high z due to shocks as the gas enters the filaments, and due to the virialization within subhalos, delineating the clumpiness along the filaments. By $z \sim 12$, T reaches $\sim 10^4$ K in the most prominent virialized centers. The web structure becomes 'illuminated' by $z \sim 8$. Fig. 14 shows the gas T within the central 400 kpc of the prime halo. At later z, the feeding filaments are clearly visible because of their lower gas temperature — the smooth (i.e., unresolved) gas component accompanies the subhalos as they penetrate to the center along the filaments like beats on the wire. The filaments extend from the computational boundaries to the very central region. The typical inflow velocity along the filaments scales roughly as the free-fall velocity, i.e., $v_{\rm ff} \sim R^{-1/2}$ within $R_{\rm vir}$ and is measures in 100s km s^{-1} in the central regions. The filaments weaken after $z \sim 2$.

Next, we calculate the baryon fraction with respect to the DM, $f_{\rm bary}$. Initially, in the WMAP3 Universe $f_{\rm bary} \sim 17\%$. The distribution of mass among the components within $R_{\rm vir}$ as a function time is shown in Fig. 15. At $z = 0$, the DM mass in the BDM prime halo is $M_{\rm vir} \sim 3.2 \times 10^{12}\ M_\odot$, the gas $\sim 1.1 \times 10^{11}\ M_\odot$ and stars $\sim 4.2 \times 10^{11}\ M_\odot$. Hence the final $f_{\rm bary} \sim 17\%$ is close to the initial ratio. Moreover, most of the time $f_{\rm bary}$ is even higher, reaching its peak of $\sim 22\%$ toward the end of the major merger epoch. We discuss the implications in §6. Here we note that the spheroidal *stellar* halo component which forms as a result of subhalo dissolution in the central region has a steep density profile of $\sim (R/10\ {\rm kpc})^{-3.5}$. Its mass contribution to the halo is not large.

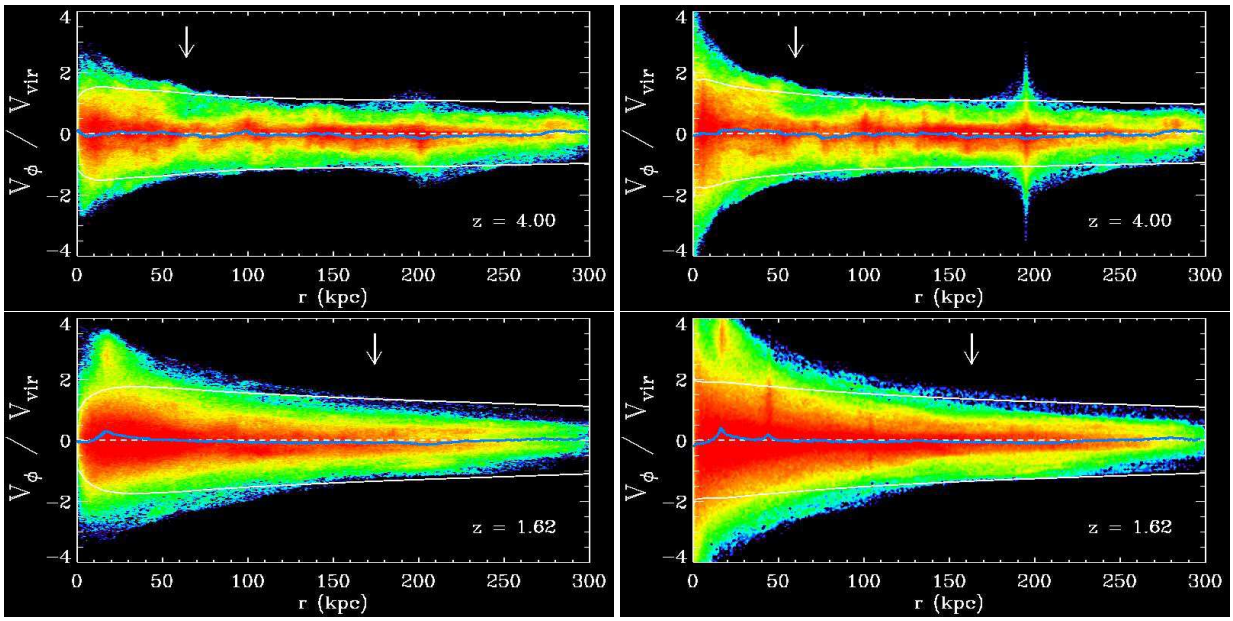

FIG. 12.— Example of evolution of the DM halo in PDM (left) and BDM (right) models, shown in the $r - v_\phi$ diagram at following times: $z = 4$ (the major merger epoch), and $z = 1.625$ (minor merger event). The colors correspond to the DM particle density on the $r - v_\phi$ surface. The white solid lines display the circular velocities in the halo as a function r at each z. The blue line shows the average v_ϕ at r. The vertical arrows show the position of $R_{\rm vir}$. The velocity axis is normalized by $v_{\rm vir}$ — the circular velocity at $R_{\rm vir}$.

The evolution of the mass ratios within the central 10 kpc is shown in Fig. 16. This is the region which hosts a stellar/gaseous disk[6] whose detailed properties are outside the scope of this work (e.g., Romano-Diaz et al. 2008c). The stellar/DM ratio reaches unity by $z \sim 2$ and is just below 2 at $z = 0$. The baryons are concentrated in the disk by $z \sim 3$, but disk/baryon ratio declines to about 0.8 at later times, reflecting the formation of a spheroidal baryonic component of stars and some hot gas. By $z \sim 0.5$, the central 10 kpc loses most of its gas component (except in the central 1–2 kpc), which is associated with a decline of the SF in the disk to $\sim 1 M_\odot$. The disk itself appears nearly gasless by the end.

We note that the *initial* disk morphology reflects the prevailing asymmetry of the background DM gravitational potential which is nonaxisymmetric. This leads directly to the formation of an asymmetric gas disk which gives rise to the stellar/gaseous bar during the first Gyr (Romano-Diaz et al. 2008c). The disk is rebuilt during the major merger epoch and experiences a number of interactions with the subhalos. A long-lived stellar bar is triggered by one of the prograde encounters. This bar drives a radial gas inflow in the disk, fueling the SF activity in the central kpc or so.

Fig. 17 shows the evolution of cold, $T \lesssim 3 \times 10^4$ K, gas fraction (of the overall gas content) within the inner 20 kpc disk region, 100 kpc and $R_{\rm vir}$. The cold gas inside $R_{\rm vir}$ is decreasing monotonically until $z \sim 0.5$, then levels off for the rest of the simulation, reflecting the gas accretion rates along the filaments. At smaller characteristic radii, this gas fraction behaves differently. Within 100 kpc it is steady till $z \sim 0.8$, well beyond the major merger epoch, then sharply declines and stabilizes. Most interestingly, the cold gas fraction within the disk region grows dramatically from $\sim 30\%$ at $z \sim 5$ to about 90% at $z \sim 0.8$. A sharp decline to $\sim 25\%$ is well correlated with the cutoff in gas accretion via filaments and a splash in the inflow rate of subhalos (Romano-Diaz et al. 2008b). Toward $z = 0$, this fraction is around 45%, but the overall gas content in this region is small, already driven out by the minor interactions with the substructure. Hence about 2/3 of the cold gas residing in the disk at $z \sim 0.7$ is driven out by the interactions. The remaining 1/3 is largely used up in star formation.

The behavior of the hotter, $T \gtrsim 3 \times 10^4$ K, gas which is not confined to the disk, but constitutes the spheroidal component mimics the evolution of the DM there in many ways (Fig. 18). While the total amount of this gas inside $R_{\rm vir}$ (which grows with time) is nearly constant in time, it is steadily declining after $z \sim 3$ at any fixed radius. This decline extends beyond the major merger epoch. If one relies on Figs. 16 and 17 to estimate the heating effect of mergers, the integral contribution of minor mergers in heating this gas and driving it out appears similar to that of the major mergers.

We have estimated the stellar mass distribution in the final disk, using vertical half-thickness of 2.5 kpc, and find that the disk contribution to the rotation curve dominates within 12 kpc. The final disk-to-virial mass ratio in the halo is $\sim 7\%$. Detailed study of disk dynamics is outside the scope of this paper, however we make a few related comments. First, the disk has lost most of its gas, $\sim 2/3$, during the late quiescent epoch when it was experiencing frequent interactions with the subhalos and the gas accretion has ceased. (The rest of the cold

[6] We define the gas (stellar) disk by determining the rotation axis of gas (stars) within the central 5 kpc. Within the equatorial plane we determine the surface density, and radial and vertical density distributions, etc.

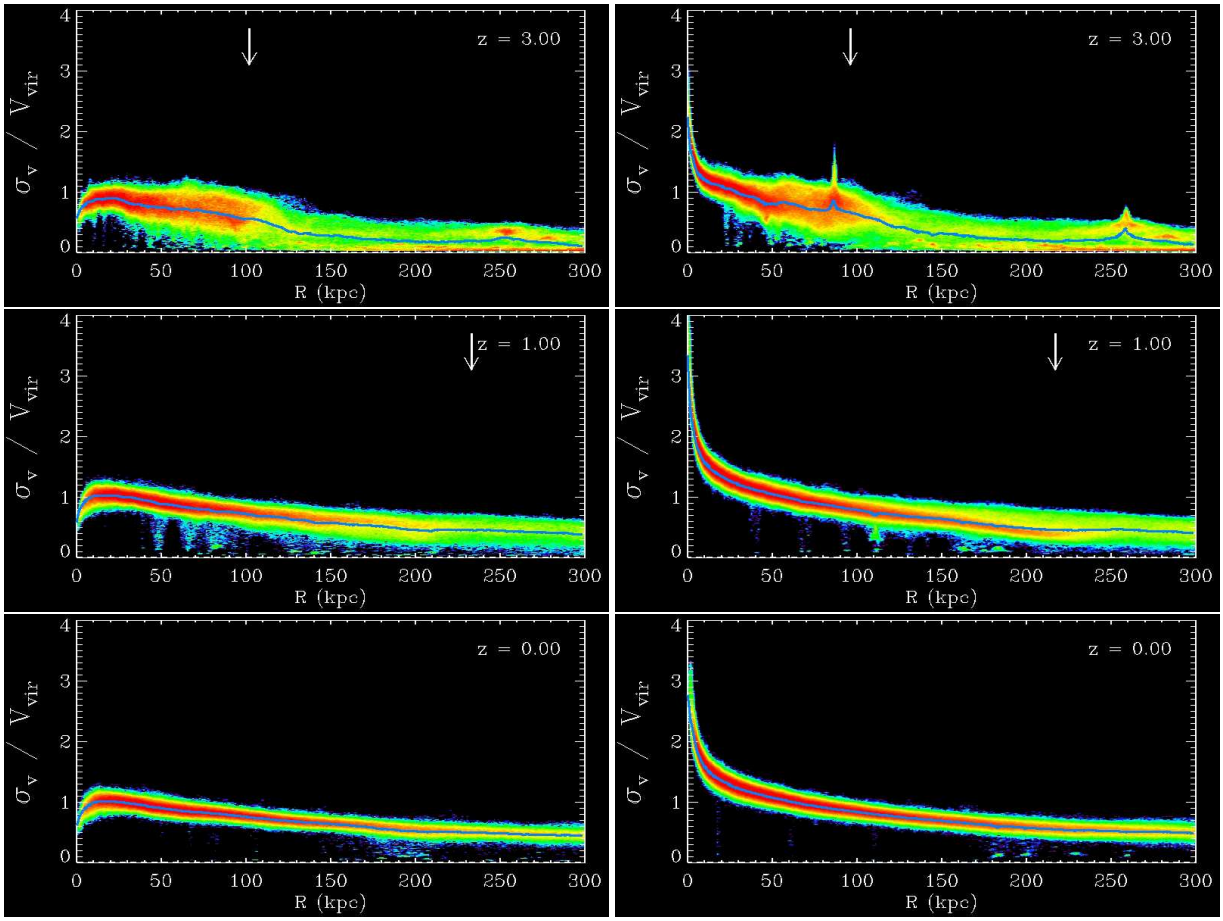

FIG. 13.— DM dispersion velocity in PDM (left) and BDM (right) models at various z. The colors correspond to DM particle densities. The y-axis is normalized by the circular velocity at $R_{\rm vir}$ at $z = 0$. The blue lines show the average values of dispersion velocities at each R and the colored width represents a 1σ dispersion around the mean. The velocity axis is normalized by $v_{\rm vir}$ — the circular velocity at $R_{\rm vir}$.

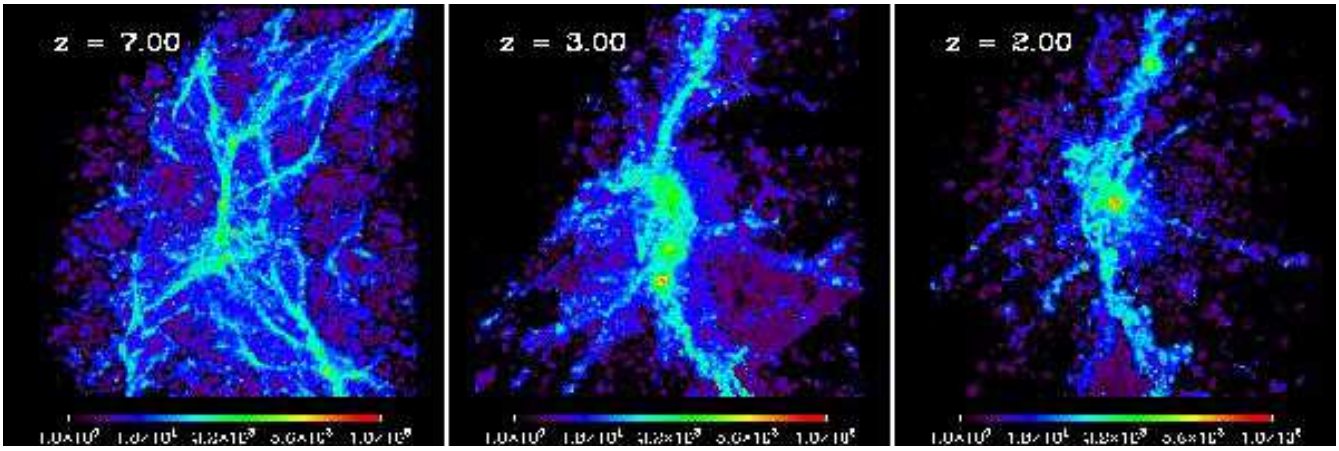

FIG. 14.— Evolution of gas temperature within the central ~ 400 kpc (as of $z = 0$) of the prime halo at $z = 7$, 3 and 3.

gas was converted into stars.) This loss of the cold gas is reflected by the decline in the SF rate by a factor of 10 (e.g., Fig. 5 of Romano-Diaz et al. 2008c). The *decline in SF rate by a factor of* ~ 10 *is a consequence, of this interaction process which drives the gas away from the disk*. Hence, the dramatic fall in the SF rate does not result from the gas conversion into stars. Second, after $z \sim 0.5$ the disk has been also losing its stellar component which was heated up due to the same interactions. This can be see in Fig. 16 (mid-frame), where stellar (and total) disk/baryon ratio within the central 10 kpc declined. We have not attempted the disk-bulge-

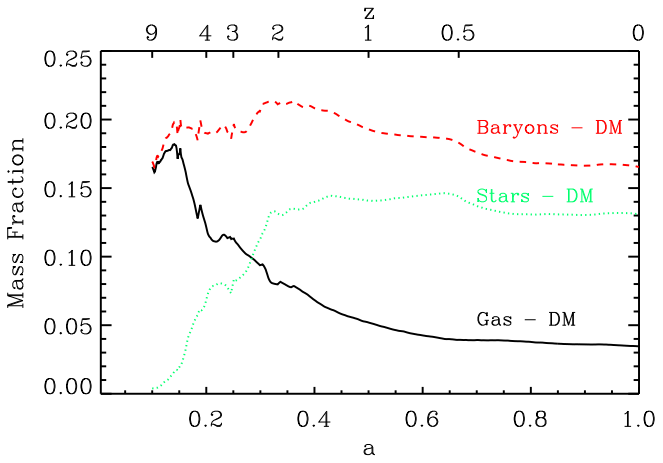

FIG. 15.— Evolution of gas, stars and baryonic fraction within $R_{\rm vir}$ of the prime halo. The ratios are given with respect to DM.

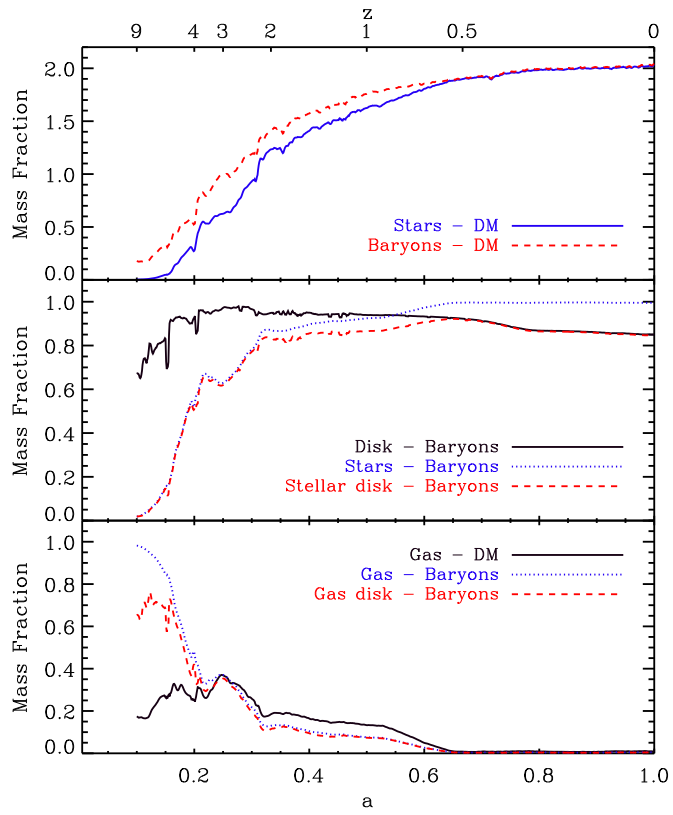

FIG. 16.— Evolution of mass ratios within the central 10 kpc: stars/DM and baryons/DM (top), disk/baryons, stars/baryons and stellar disk/baryons (middle), and gas/DM, gas/baryons and gas disk/baryons (bottom).

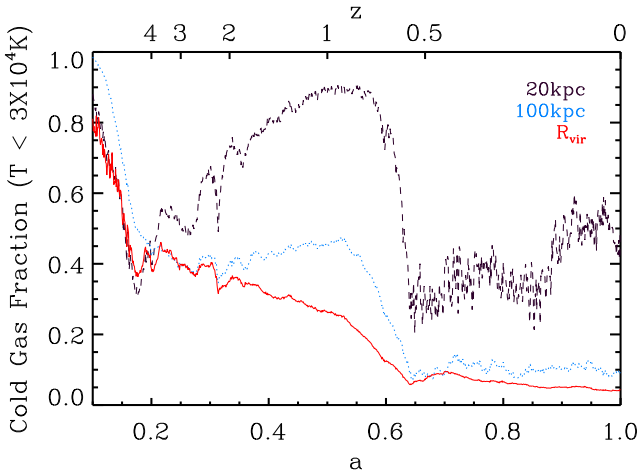

FIG. 17.— Evolution of cold, $T \lesssim 3 \times 10^4$ K, gas mass fractions (of the total gas within R) within the central 20 kpc, 100 kpc and $R_{\rm vir}$ of the prime halo. The fractions are normalized by the total gas mass within the same radius. Note, that the 100 kpc curve lies outside $R_{\rm vir}$ for $z \gtrsim 3$.

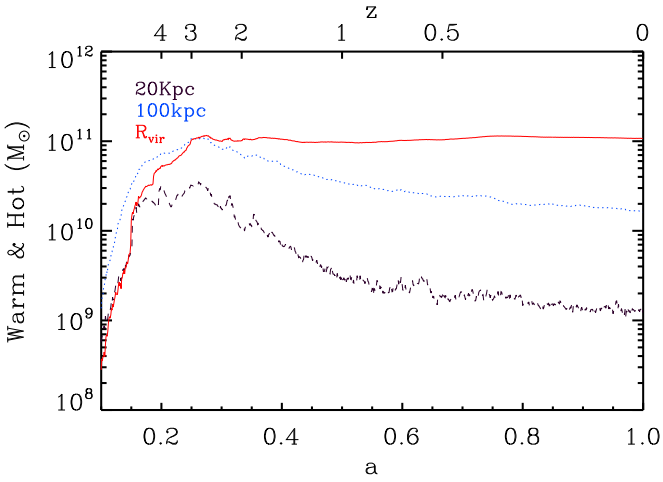

FIG. 18.— Evolution of warm and hot, $T \gtrsim 3 \times 10^4$ K, gas mass within the central 20 kpc, 100 kpc and $R_{\rm vir}$ of the prime halo. Note, that the 100 kpc curve lies outside $R_{\rm vir}$ for $z \gtrsim 3$.

bar decomposition, but use the mass ratio of the *stellar* spheroidal component to stellar disk within the disk radius. This ratio has increased with time from 0.1 at $z \sim 2$, to 0.2 at $z \sim 1$, to 0.7 at $z = 0.5$. In tandem with the gas loss from the disk, this hints at morphological evolution from late Hubble type to intermediate and early type disk.

A new and potentially interesting mechanism of truncating the stellar disk was noticed. At various times, highly inclined and massive gaseous rings have been spotted to form around the disk, with radii $\sim$ 15 – 20 kpc. They did not evolve into polar rings (e.g., Sparke 2002), appear short-lived and related to the gas accretion through the filaments. No attempt was made to quantify their effect on the disk dynamics, but they are expected to exert substantial perturbarions on the *direction* of the angular momentum vector in the disk region (see below).

We have calculated the evolution of angular momentum in the gas and stars and compared it with that of the DM at various spatial scales. Prior to $z \sim 3$, the orientation of the total $J_{\rm DM}$ correlates nicely with that of the total $J_{\rm gas}$ inside $R_{\rm vir}$, while this radius is well below 100 kpc (Fig. 19a). After $z \sim 1$, the gas appears to counter-rotate at high inclination to the DM globally. At this time almost all the gas is hot, $T \gtrsim 3 \times 10^4$ K, within $R_{\rm vir}$. The global gas and stellar J are aligned only

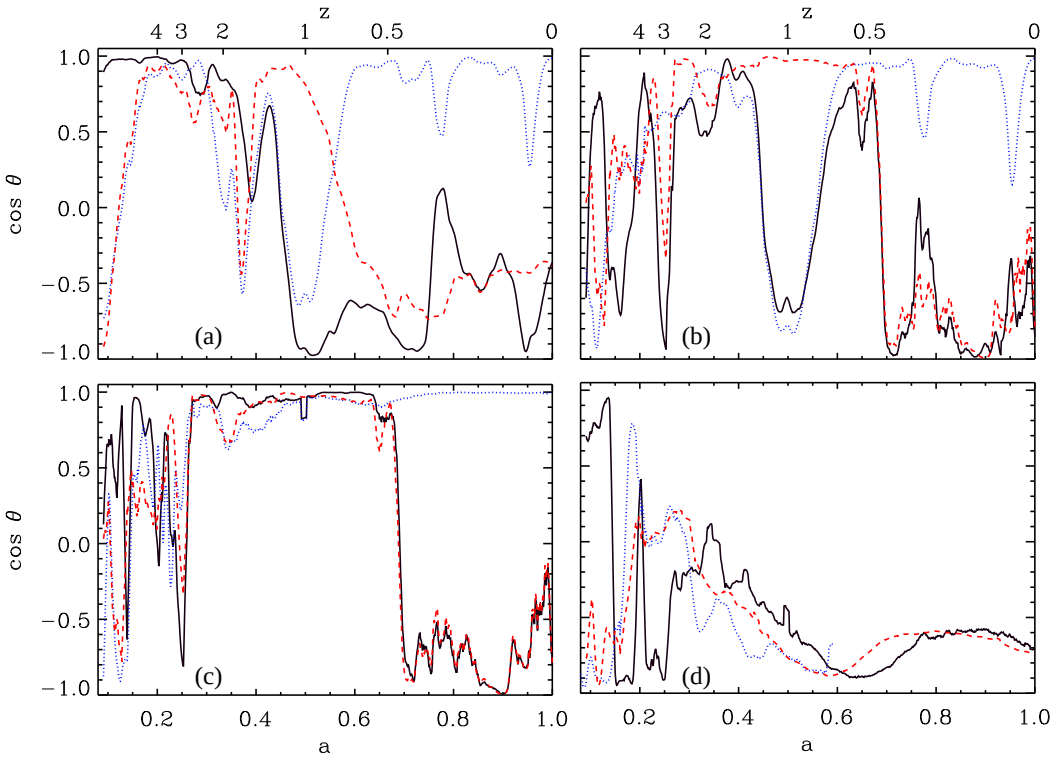

FIG. 19.— Correlations between angular momenta of the DM, gas and stars within (a) $R_{\rm vir}$, (b) $R_{\rm vir}$ (DM) and 8 kpc (gas and stars), and (c) 8 kpc (DM, gas and stars). The angle θ is defined between the corresponding J's. The colors are those of DM–gas (black, solid), DM–stars (blue, dotted) and stars-gas (red, dashed). (d) The orientation of J's within the central 8 kpc with respect to the inertial frame. The colors are those of DM (black, solid), gas (blue, solid) and stars (red, dashed).

between the major mergers and around $z \sim 1-1.7$. This alignment occurs when the gas disk is dominated by the cold gas component.

When global (i.e., within $R_{\rm vir}$) $J_{\rm DM}$ is contrasted with $J_{\rm gas}$ and $J_{\rm gas}$ within the disk region of inner 8 kpc (Fig. 19b), the correlation between DM and stars, and DM and gas becomes much better after the major mergers and before the cold gas is ablated from the disk. When all J's are limited to within the central 8 kpc (Fig. 19c), the correlations between the components become even better. Interestingly, the cold gas that is concentrated within the central 1–2 kpc after $z \sim 0.5$ anticorrelates with DM and therefore anticorrelates (i.e., counter-rotates) with stars as well.

After the stellar disk formation, its rotation axis experiences an oscillatory motion within respect to the fixed inertial system of coordinates and is closely followed by the DM axis within the same region. This trend is interrupted by the mergers but always returns (Fig. 19d).

6. DISCUSSION AND CONCLUSIONS

We have compared the buildup of DM halos with and without baryons, BDM and PDM respectively, from identical cosmological initial conditions. As a template, we choose to follow the evolution of massive, Milky Way-type halos which emerge from their major merger phase early, by $z \sim 1.5$, and remain isolated thereafter. We have followed the evolution of characteristic quantities in the halos, i.e., $\tilde{R}_{\rm s}$ ($\equiv \gamma R_{\rm vmax} \sim 0.46 R_{\rm vmax}$), $R_{\rm vmax}$, $R_{\rm vir}$, the radial density distribution, the bound fractions, the phase-space distribution function, figure tumbling, and the full and specific angular momenta. Furthermore, we have analyzed the halo relaxation in the configuration and phase spaces and again compared how this process is affected by baryons. We find that following the evolution of DM accretion in the $R-v_{\rm R}$ and $r-v_\phi$ planes allows one to observe and quantify the development of substructure within the halo — the subhalos, tidal tails and streamers. Finally, we comment on the baryon buildup within the halo (see also Romano-Diaz et al. 2008b,c). The quantitative evolution of the substructure is further analyzed in Paper II.

The resulting PDM and BDM halos have been compared to the halo distribution in the $M_{\rm vir}-z_{\rm form}$ plane for the Types III and IV halos of McBride et al. (2009), where $z_{\rm form}$ is the halo formation time using McBride et al. definition. They deviate in about 2σ from the mean that was obtained by compiling an extensive catalog of $\sim 500,000$ halos from the Millenium simulation. Types III and IV, together are the most significant population of halos. Moreover, our halos lie within $1\sigma - 2\sigma$ from the mean in Li et al. (2007) who studied the Mass Accretion Histories (MAHs) of DM halos in large cosmological boxes. This lowers our halos probability accordingly, but they remain plausible. In the mass range of 10^{12-13} $M_\odot$ in Li et al., the probability distributions of halo properties sample objects with only a few 100 particles, making it difficult to reliably estimate the width of the distribution. But it seems that our DM halos grew faster than MAHs from Li et al. show, by a factor of ~ 2, during the major merger epoch. The reason for this is explained in §3.1 and has no effect on the actual

evolution.

As a next step, we attempt to understand our results presented in §3–5. The prime halo accumulation in these simulations happens in the loose field rather than in the dense cluster environment because the forming halo is embedded in the region whose overdensity is zero. The number of major mergers in the system is determined by the random component of the CRs. We first compare the key parameters of PDM and BDM model halos. The halos have nearly the same mass within their virial radii, but the large-scale mass distribution in both models differs in its degree of triaxiality. As expected, the BDM model ends up much less triaxial, being nearly axisymmetric and somewhat flattened. The evolution of the innermost mass distribution diverges in both cases as well. While the PDM halo quickly acquires the NFW cusp with $\rho \sim R^{-1}$ and a stable $R_{\rm s}\sim$ 28 kpc after the epoch of major mergers, the BDM halo develops an isothermal cusp with $\rho \sim R^{-2}$, bypassing the NFW cusp (Romano-Diaz et al. 2008b). The isothermal cusp is stable between $z \sim 1-4$ and is gradually erased thereafter, leading to the formation of a flat DM core in the central 2–3 kpc. The reason for this behavior is two-fold: first, the adiabatic contraction is initiated by the dissipative baryons, dragging the DM inwards. The major mergers do not affect the $\log\rho-\log R$ slope of –2 for the DM mass distribution. However, the subsequent minor mergers penetrating the inner 20–30 kpc are accreted in groups of a few because the subhalos cluster already during their motion along the filaments. Not only their dynamical friction affects the isothermal DM cusp but they also have a profound effect on the baryons in the cusp, when the cold disk gas is ablated and, together with the inner halo hot gas, is driven out.

The diverging evolution of PDM and BDM halos is also demonstrated by their concentration parameter $\tilde{c}$ (Fig. 4). The latter halo is much more concentrated because of the smaller $\tilde{R}_{\rm s}\sim$ 15 kpc vs $\tilde{R}_{\rm s}\sim$ 28 kpc in the PDM. The abrupt change in the growth of $\tilde{c}$ after $z \sim 0.5$ is closely associated with the minor mergers and clustering of accreted subhalos, coming from the filaments.

In phase space, we find that the phase space density, $Q(R)$, of the DM in the BDM model cannot be fit by a power law, unlike in the PDM model. The differences appear in the central $\sim$ 30 kpc, as a downward trend after $z \sim 4$. After $z \sim 0.5$, the central Q drops even faster and $Q(R)$ flattens within the central few kpc (Fig. 5). This can be related to the formation of an isothermal density cusp there between $z \sim 4-1$ and its gradual flattening from inside out after this time. This means that the entropy per DM particle, defined as $\sigma^2_{\rm DM}\rho^{-2/3}$ (e.g., Hoffman et al. 2007), increases in the central region of the BDM halo compared to the PDM.

Both PDM and BDM halos show very little figure tumbling with respect to any axis (Fig. 6), based on $\sim$ 900 snapshots. This happens despite some DM particles acquiring substantial angular velocities with respect to the halo CoM. The cosmological λ falls within the limits normally attributed to the halo angular momentum, $\lambda \sim 0.01-0.1$. The angular momentum of the halo during its assembly is channeled into the internal circulation of DM particles and not into the tumbling of their orbits in any collective fashion. By internal circulation we mean J associated with individual orbits which may or may not correlate among themselves. If they do, the halo will possess a net J (i.e., λ), but its figure can remain stationary nevertheless.

The halo figure tumbling was claimed to be insignificant, if evolved in a small isolated box or for cluster mass halos (e.g., Dubinski 1992; Bureau et al. 1999). Heller et al. (2007) found that, for a large number of galactic halo models with and without baryons evolved in isolation from high z, the resulting halo figures tumble exceedingly slow, with an average $\Omega_{\rm h} \sim 0.2$ km s^{-1}kpc^{-1} around their minor axes. This agrees nicely with Bailin & Steinmetz (2004) estimates from 4 snapshots for halos extracted from cosmological simulations. A departure from axial symmetry, especially during the early epoch, taken in tandem with the exceedingly slow tumbling of the halo figure has important *dynamical* consequences for the growing baryonic disk. The simplest explanation to the absence of tumbling in the PDM and BDM halos comes from the tidal effects of the large-scale DM filaments. This is confirmed by the stable orientation of the halo major axis with respect to the filament. The same effect is more difficult to understand in the context of isolated halos with angular momentum inserted via initial conditions (Heller et al. 2007).

The evolution of angular momentum associated with spherical shells within DM halo is complex, but the observed increase in $J(\tilde{R}_{\rm s})$ and $j(\tilde{R}_{\rm s})$ of the BDM halo compared with the PDM is a signature of an angular momentum transfer from the massive disk in the innermost halo. We also detect changes in the position angle of the total angular momentum $\vec{\mathbf{J}}(R_{\rm vir})$ of the halo, both in the PDM and BDM models, while their value is stable. The change in the orientation of J is much easier to achieve than the change in its value.

Potentially interesting are the correlations between the angular momenta of baryons (stars and gas) and DM, shown in Fig. 19 as an angle between the pairs of J's. On the scale of $R_{\rm vir}$, $J_{\rm DM}$ is aligned with $J_{\rm gas}$ untill $z \sim 3$, and largely anticorrelates (anti-aligned) at $z \sim 1-0.5$ (Fig. 19a). The picture differs when the disk region baryons are correlated with the DM within $R_{\rm vir}$ — abrupt changes occur during the mergers (Fig. 19b). The best correlation is obvious when all components are compared within the disk region — the DM and gas J's are oriented similarly here between $z \sim 3-0.5$ and then abruptly anticorrelate (counter-rotate) at later times, when the cold gas is limited to the central kpc (Fig. 19c).

Of course no correlation is maintained between $J_{\rm DM}$ within $R_{\rm vir}$ and $J_{\rm stars}$ within the stellar disk during mergers. Even during the quiescent epoch, $z \sim 1$, the disk experiences a flip-flop (i.e., from corotation with the halo DM to counter-rotation and back, Fig. 19b). This can be most probably related to the interactions with the streamers which survive for a long time, see below.

An important issue when analyzing the growth of a DM halo is how the DM and baryons are deposited within its volume — this brings us to the question of internal relaxation. The halo experiences virialization — a particular relation between its kinetic and potential energies is achieved. This process is typically associated with a time-dependent gravitational potential. Clearly, the halo acquires a degree of virialization only asymptotically, as

the rate of major mergers subsides. While virialization proceeds on a dynamical timescale, its incompleteness is related to the halo being an open system, accreting from its environment.

The relaxation process extends beyond virialization and continues both in the configuration and phase spaces. In the former, we ask how was the halo assembled. Did its central part, say within $\tilde{R}_{\rm s}$, form early in its evolution, e.g., during the major merger epoch, as advocated by Wechsler et al. (2002), and does the presence of baryons make any difference in this process? How quickly the substructure evolves within $R_{\rm vir}$? (By substructure we mean subhalos, their tidal tails and streamers, as defined in §4.) In the latter, we ask how long the position-velocity correlations persist after dissolution of the bound structures (subhalos) within the halos, and again, do baryons have any effect on this process?

We start by comparing some details of radial mixing of DM halos and a non-singular 'isothermal' sphere (NSIS). The fractions of 'bound' particles — those limited in their radial motion to within a specific radius by their energy are shown in Fig. 7, where R-axis was normalized by $R_{\rm vmax}$. After the epoch of major mergers, the fractions of bound particles, η, within R stay constant with time. We see that the fraction of bound particles within $\sim R_{\rm vmax}$ is substantially higher in the PDM and BDM halos compared to NSIS, while outside this radius it is nearly the same. Hence, particles of the NSIS found within $R_{\rm vmax}$, will perform larger radial excursions than those found in the modeled halos. In this region, the BDM and PDM halos are more bound than NSIS. But even with this higher fraction in the BDM halo η is still only $\sim 23\%$ within $R_{\rm vmax}$, $\sim 15\%$ within $\tilde{R}_{\rm s}$, declining sharply (faster than in the NSIS) within $\tilde{R}_{\rm s}$, and even faster within the NFW cusp of the PDM and the flat density core of BDM. Inside the cusp, η drops well below 1%. This means that the majority of particles in the PDM and BDM halos, at virtually every radius inside $R_{\rm vmax}$, are not confined within their current R, especially in the central regions. Hence we cannot confirm that particles accreted during the major mergers form the core of DM halos. The part of the PDM and BDM halos inside $R_{\rm vmax}$ must be well mixed. Energy considerations provide a relatively weak constraint on the motions of DM particles within this region.

The fraction of *bound* particles, albeit small, within $R_{\rm vmax}$ assemble within the major merger epoch, in PDM and BDM models. How can this be reconciled with the DM density profiles which are believed to form in the early stage of evolution? While the fractional contribution of (minor) subhalos is insignificant within $R_{\rm vmax}$ in both PDM and BDM, their fate differs substantially. The analysis of Paper II (see also Romano-Diaz et al. 2008c) shows that many of the PDM subhalos are tidally destroyed before they enter $\tilde{R}_{\rm s}$, while the BDM ones, 'glued' by baryons, survive the radial plunge. It is important that the flow of the *unbound* DM contributes about $80-90\%$ of the DM within $\tilde{R}_{\rm s}$ after the merger epoch, but *the net influx of this material is zero,* and this region appears to be in a steady state (Fig. 8). Most of the DM particles within $\tilde{R}_{\rm s}$ reside there for a short crossing time only.

Next, we analyze the relaxation of DM particles and their substructures in the $R-v_{\rm R}$ and $r-v_\phi$ planes. The general framework of halo assembly is that of the background filamentary structure which triggers the DM and baryon flow. As discussed in §4, this process is accompanied by violent relaxation whose efficiency depends on the presence of substructure, and especially the residual currents in the halo which continue to 'mix' the halo environment even in the absence of large-amplitude variability in the central potential. Fig. 10 (and Animation Seq.) phase diagrams delineate the DM substructure in the various stages of its evolution. The prime halo and subhalos are more centrally concentrated with baryons, and the 'fingers' are much more pronounced in this case. Note the difference in the shape of $v_{\rm R}$ at small R in Fig. 10 and especially in the central 20 kpc between the PDM and BDM models — the DM potential is flat in the former and cuspy in the latter model, as can be also be seen in the dispersion velocity maps (Fig. 13). The development of the flat core after $z\sim 1$ in the prime halo does not reverse this trend. The absence of such cores in the subhalos is most probably related to the numerical resolution. Especially revealing are the later time frames which show that even after the subhalos disintegration a substantial correlation in the position-velocity diagram (i.e., streamers) remains within $R_{\rm vir}$ up to $z=0$. Furthermore, as we discuss in Paper II, shells of tidally disrupted DM material travel outside $R_{\rm vir}$ and remain there at present. After $z\sim 1$, we find that the outflowing material can cross ~ 1 Mpc distance from the prime halo.

There are a few ways to quantify the substructure presence within $R_{\rm vir}$. Here we attempted to smooth the halo DM in $R-v_{\rm R}$ and $r-v_\phi$ planes and use it as a (local) benchmark of the density level in the halo. Subtracting it from the actual density map and normalizing it by a reference mass $M_{\rm vir}$, we obtained the excess mass fraction associated with the substructure. This mass-conserving procedure smears large density gradients in the phase-space. Fig. 11 shows that the substructure becomes more important with time in PDM and BDM models and is somewhat more 'visible' in the former model — a result which seems to be counter-intuitive. The simplest explanation of this phenomena lies in the accumulation of streamers with time in both models and the more efficient mixing in the BDM model. The characteristic orbital time at ~ 200 kpc is ~ 2 Gyr. Assuming that a few orbits are essential for efficient mixing, the streamers that have been produced before $z\sim 1$ are expected to disappear by $z=0$. Streamers produced later on, most likely will survive to the present.

When analyzing the evolution of global and innermost mass fractions (Figs. 15 and 16), we find that the baryon/DM fraction, $f_{\rm bary}$, within $R_{\rm vir}$ increases during the major merger epoch and decreases during the quiescent period. One should be cautious not to over-interpret the final value of $f_{\rm bary}$ being so close to its initial value. The crucial point here is the level of feedback from stellar evolution which drives the baryons out of the halo. Our models have been fine-tuned and used the feedback values from Heller et al (2007b). They are based on a large number of simulations where the effects of the main free parameters in the SF have been investigated. We have observed that an increase in the feedback results in smaller bulge-to-disk mass ratios, while its decrease has

led to extremely bulge-dominated models. The adopted values were those that led to the best correspondence of the final disks to those observed. It is interesting that our choice resulted here in a near conservation of baryons within $R_{\rm vir}$ in the BDM model.

We now turn again to the baryon assembly within the DM halo. Most of the baryon influx into the halo is channeled along the filaments (e.g., Keres et al. 2005; Ocvirk et al. 2008; Dekel et al. 2009) as a low angular momentum gas (Fig. 14). While we avoid here discussing the disk dynamics (e.g., Romano-Diaz et al. 2008c), we do focus on the parameters which characterize some aspects of the baryon accumulation within the halo, especially within the central 10 kpc and a larger disk region. Within 10 kpc, the stars dominate over DM after $z \sim 2$ and the stars/DM mass ratio tends asymptotically to ~ 2. The disk-to-total baryon mass ratio within this region tends to ~ 0.8 at present, which means that the stellar spheroidal contribution (i.e., bulge and innermost stellar halo) is $\sim 20\%$.

After $z \sim 0.5$, the disk loses its gas content, due to the highly non-steady influx of subhalos which ablate the cold disk gas (see also Romano-Diaz et al. 2008b,c and 2009a for more details). From the history of cold, 3×10^4 K, and hot gas mass fractions within the central 20 kpc (Figs. 17 and 18), we note that the hot gas residing in the spheroidal component and corresponding stars expand as a result of the subhalo heating of the immediate disk region. Within the larger disk region, ~ 15 kpc — 20 kpc, the ratio of stellar spheroidal component to the total stellar disk mass increases with time, from 0.1 at $z \sim 2$, 0.2 at $z \sim 1$, to 0.7 at $z \sim 0.5$. This trend of increasing disk/spheroid stellar mass ratio is consistent with evolution toward an early-type spiral galaxy. Similar evolution was described by Naab et al. (2007) for one of their models, model E.

The 'cold' baryons ending up in a disk in the BDM model have resulted in $M_{\rm disk}/M_{\rm vir} \sim 7\%$. In comparison, Xue et al. (2008) quote $M_{\rm disk}/M_{\rm vir} \sim 6.5\%$ for the Milky Way galaxy, with $M_{\rm disk} \sim 6.5 \times 10^{10}$ M$_\odot$ and $M_{\rm vir} \sim 10^{12}$ M$_\odot$, but higher estimates for the MW disk exist as well, e.g., 8×10^{10} M$_\odot$. Hence, our halo-to-disk mass fraction fits within this range.

Conroy et al. (2007) quotes a higher halo-to-stellar mass ratio for the total stellar masses in excess of $10^{11} h^{-2}$ M$_\odot$, using different definition for the halo mass. We find that, after accounting for these differences, a factor of 8 remains with their mean value, and a factor of 4 within their 1σ. Interestingly, the quoted above results for the MW, will differ by the same factor with Conroy et al. We do not find that this difference will affect the processes discussed here, because wew compare identical halos with and without baryons.

To summarize, in a number of associated publications, we have compared the evolution of DM halos with and without baryons, from identical initial conditions. Here we focus on two issues: assembly of the prime halos and their relaxation processes. We find that baryons contribute decisively to the evolution of the cusp region, with the baryon model leading to the formation of an isothermal DM cusp, due to an adiabatic contraction. This cusp was ultimately dissolved by interactions with the DM+baryon substructure and formed a flat density core (see also Romano-Diaz et al. 2008b). The DM halo in this model nevertheless remained more centrally concentrated compared to the pure DM model. Futhermore, we find that the epoch of minor mergers is actually dominated by interactions with the subhalos (with and without baryons). These are responsible for ablating the cold, $< 3 \times 10^4$ K, gas component from the embedded disk, as well as heating up the innermost halo gas and stars, causing their expansion out of the region. Heating the spheroidal gas, stellar and DM components in the inner halo is the result of dynamical friction by the subhalos. The disk, which started as gas dominated, becomes an intermediate Hubble type by $z \sim 2$, and resembles that of the lenticular galaxies after $z \sim 0.5$. The spheroidal-to-disk stellar mass ratio is ~ 0.7 at this z (within the disk radius), and the disk spiral activity has ceased accordingly, except during interactions with the subhalos.

Analyzing the halo assembly history we find that only a small, $\sim 11 - 15\%$, fraction of DM particles within $\tilde{R}_{\rm s}$ and $\sim 17 - 23\%$ within $R_{\rm vmax}$, in PDM and BDM models respectively, are bound to within these radii — most of the DM particles perform much larger radial excursions, thus mixing the smooth fraction of the inner halo particles. We compare this behavior with that of a non-singular isothermal sphere in equilibrium. While the bound DM particles assemble early within these radii, the fraction of bound particles is small at all times. In other words, the mass distribution within $R_{\rm vmax}$ is defined by DM particles which freely stream across this region.

Lastly, the halos are only partially relaxed beyond their virialization. Being an open system and accreting a substantially inhomogeneous material (in all combinations of DM and baryons), the degree of mixing in the halo is limited — although bound subhalos are tidally disrupted, their debris preserve correlations in the phase-space over a few Gyrs time. The mixing process becomes even less efficient with time and phase-space correlations (streamers) formed after $z \sim 1$ largely survive intact to the present. Hence the halos are virialized but not 'thermalized.' This has interesting implications for the disk evolution and we explore them in subsequent publications (Romano-Diaz et al. 2008b,c, 2009a). The persistence of substructure well past the virialization assures that the trend toward a more complete violent relaxation does not cease, but no attempt to quantify this process here.

Discussions with John Dubinski, Shardha Jogee and Simon White are gratefully acknowledged. We thank Ingo Berentzen for help with visualizations, and Jorge Villa-Vargas and Miguel A. Aragon-Calvo for helpful discussions on numerical issues. This research has been partially supported by NASA/LTSA/ATP, NSF and STScI to I.S. STScI is operated by the AURA, Inc., under NASA contract NAS 5-26555. I.S. is grateful to the JILA Fellows for support. Y.H. has been partially supported by the ISF (13/08).

REFERENCES

Allgood, B., Flores, R.A., Primack, J.R., Kravtsov, A.V., Wechsler, R.H., Faltenbacher, A., Bullock, J.S. 2006, MNRAS, 367, 1781

Athanassoula, E., Misiriotis, A. 2002, MNRAS, 330, 35

Athanassoula, E. 2002, ApJ, 569, L83
Bailin, J., Steinmetz, M. 2004, ApJ, 616, 27
Barnes, E.I., Williams, L.L.R., Babul, A., Dalcanton, J.J. 2007, ApJ, 654, 814
Barnes, J., Hut, P. 1986, Nature, 324, 446
Berentzen, I., Shlosman, I. 2006, ApJ, 648, 807
Bertschinger, E. 1987, ApJ, 323, L103
Bryan, G.L., Norman, M.L. 1998, ApJ, 495, 80
Bullock, J.S., Dekel, A., Kolatt, T.S., Kravtsov, A.V., Klypin, A.A., Porciani, C. & Primack, J.R. 2001, ApJ, 555, 240
Bureau, M., Freeman, K.C., Pfitzner, D.W., Meurer, G.R. 1999, AJ, 118, 2158
Christodoulou, D.M., Kazanas, D., Shlosman, I., Tohline, J.E. 1995, ApJ, 446, 472
Conroy, C. et al. 2007, ApJ, 654, 153
Debattista, V.P., Sellwood, J.A. 1998, ApJ, 493, L5
Dehnen, W. 2001, MNRAS, 324, 273
Dehnen, W. 2002, J. Comput. Phys., 179, 27
Dekel, A. et al. 2009, Nature, 457, 451
Diemand, J., Kuhlen, M., Madau, P. 2007, ApJ, 667, 859
Diemand, J., Kuhlen, M., Madau, P., Zemp, M., Moore, B., Potter, D., Stadel, J., 2008, Nature, 454, 735
Dubinski, J. 1992, ApJ, 401, 441
Dubinski, J. 1994, ApJ, 431, 617
Eisenstein, D.J. & Hut, P. 1998, ApJ, 498, 137
El-Zant, A. 2008, ApJ, 681, 1058
Gao, L., De Lucia, G., White, S.D.M., Jenkins, A. 2004a, MNRAS, 352, L1
Gao, L., White, S.D.M., Jenkins, A., Stoehr, F., Springel, V. 2004b, MNRAS, 355, 819
Ghigna, S., Moore, B., Governato, F., Lake, G., Quinn, T., Stadel, J. 1998, MNRAS, 300, 146
Gnedin, O.Y., Kravtsov, A.V., Klypin, A.A., Nagai, D. 2004, ApJ, 616, 16
Hansen, S.H., Moore, B. 2006, New Astron., 11, 333
Heller, C.H., Shlosman, I. 1994, ApJ, 424, 84
Heller, C.H., Shlosman, I., Athanassoula, E. 2007, ApJ, 671, 226
Hoffman, Y., Ribak, E. 1991, ApJ, 380, L5
Hoffman, Y., Romano-Diaz, E., Shlosman, I., Heller, C.H. 2007, ApJ, 671, 1108
Kazantzidis, S., Kravtsov, A.V., Zentner, A.R., Allgood, B., Nagai, D., Moore, B. 2004, ApJ, 611, L73
Kennicutt, R.C. 1998, ApJ, 498, 541
Keres, D., Katz, N., Weinberg, D.H., Dave, R. 2005, MNRAS, 363, 2
Klypin, A., Gottlöber, S., Kravtsov, A.V., Khokhlov, A.M. 1999a, ApJ, 516, 530
Klypin, A., Kravtsov, A.V., Valenzuela, O., Prada, F. 1999b, ApJ, 522, 82
Li, Y., Mo, H.J., van den Bosch, F.C., Lin, W.P. 2007, MNRAS, 379, 689
Lynden-Bell, D. 1967, MNRAS, 136, 101
Lynden-Bell, D., Kalnajs, A.J. 1972, MNRAS, 157, L1
Martinez-Valpuesta, I., Shlosman, I., Heller, C.H. 2006, ApJ, 637, 214
McBride, J., Fakhougi, O., Ma, C.-P. 2009, MNRAS, submitted; arXiv/0902.3659
Moore, B., Ghigna, S., Governato, F., Lake, G., Quinn, T., Stadel, J., Tozzi, P. 1999, ApJ, 524, L19
Naab, T., Johansson, P.H., Ostriker, J.P., Efstathiou, G. 2007, ApJ, 658, 710
Navarro, J.F., Frenk, C.S., White, S.D.M. 1997, ApJ, 490, 493 (NFW)
Ocvirk, P., Pichon, C., Teyssier, R. 2008, MNRAS, 390, 1326
Porciani, C., Dekel, A. & Hoffman, Y. 2002, MNRAS, 332, 325
Reed, D., Governato, F., Quinn, T., Gardner, J., Stadel, J., Lake, G. 2005, MNRAS, 359, 1537
Romano-Diaz, E., Hoffman, Y., Faltenbacher, A., Heller, C.H., Jones, D., Shlosman, I. 2006, ApJ, 637, L93
Romano-Diaz, E., Hoffman, Y., Heller, C.H., Faltenbacher, A., Jones, D., Shlosman, I. 2007, ApJ, 657, 56
Romano-Diaz, E., Shlosman, I., Heller, C.H., Hoffman, Y. 2009a, in preparation (Paper II)
Romano-Diaz, E., Shlosman, I., Hoffman, Y., Heller, C.H. 2008b, ApJ, 685, L105
Romano-Diaz, E., Shlosman, I., Heller, C.H., Hoffman, Y. 2008c, ApJ, 687, L13
Shlosman, I. 2007, Pathways through an Eclectic Universe, J.H. Knapen, T.J. Mahoney & A.Vazdekis (eds.), ASP Conf. Ser. 390, p. 440, arXiv:0710.0630
Sparke, L.S. 2002, Disks of Galaxies: Kinematics, Dynamics & Perturbations, ASP Conf. Proc., Vol. 275. (eds.) E. Athanassoula, A. Bosma & R. Mujica, 367
Spergel, D.N., et al. 2003, ApJS, 148, 175
Spergel, D.N., et al. 2007, ApJS, 170, 377
Springel, V., Wang, J., Vogelsberger, M., Ludlow, A., Jenkins, A., Helmi, A., Navarro, J.F., Frenk, C.S., White, S.D.M. 2008, MNRAS, 391, 1685
Taylor, J.E., Navarro, J.F. 2001, ApJ, 563, 483
Tormen, G., Diaferio, A., Syer, D. 1998, MNRAS, 299, 728
Tremaine, S. & Weinberg, M.D. 1984, MNRAS, 209, 729
Wechsler, R.H., Bullock, J.S., Primack, J.R., Kravtsov, A.V., Dekel, A. 2002, ApJ, 568, 52
Weinberg, D.H., Colombi, S., Dav, R., Katz, N. 2008, ApJ, 678, 6
van de Weygaert, R., & Bertschinger, E. 1996, MNRAS, 281, 84
White, S.D.M., Rees, M.J. 1978, MNRAS, 183, 341
Xue, X.X. et al. 2008, ApJ, 684, 1143
Zait, A., Hoffman, Y., Shlosman, I. 2008, ApJ, 682, 835